UNIVERSITY OF CALIFORNIA, SAN DIEGO

Infrared micro- and nano-spectroscopy of carbon-based materials

A dissertation submitted in partial satisfaction of the
requirements for the degree
Doctor of Philosophy

in

Physics

by

Omar Khatib

Committee in charge:

Professor Dimitri N. Basov, Chair
Professor Peter M. Asbeck
Professor Massimiliano Di Ventra
Professor Sunil K. Sinha
Professor William C. Trogler

2014

The dissertation of Omar Khatib is approved, and it is acceptable in quality and form for publication on microfilm and electronically:

_____

_____

_____

_____

_____
Chair

University of California, San Diego

2014

EPIGRAPH

Science may set limits to knowledge, but should not set limits to imagination.
—Bertrand Russell

I'm sick of following my dreams. I'm just going to ask them where they're going and hook up with them later.
—Mitch Hedberg

TABLE OF CONTENTS

LIST OF FIGURES

ACKNOWLEDGEMENTS

Firstly, I would like to acknowledge and dedicate this work to my parents, Jumana and the late Ahmad Khatib. My father passed away during my time in graduate school, but his influence on how I conduct myself personally and professionally lives on. I am thankful to have been so close to my home in Los Angeles, allowing me to never lose a connection to the place I grew up, and the people responsible for allowing me to flourish. There is no single person more important to me than my mother. I feel extremely priveledged, and would be nowhere near where I am today without her unrelenting love and support.

I would like to acknowledge my advisor, Dimitri N. Basov, for molding me into the scientist I am today. Every day he sets an example of the drive, dedication, and hard work needed to be a top-tier researcher in condensed matter physics. I am indebted to him for providing me with an expansive lab with frontier instrumentation, and an intellectual playground to explore my ideas and develop a sound foundation for optical and solid state physics. I would also like to thank my thesis committee: Peter Asbeck, Max Di Ventra, Sunil Sinha, and Bill Trogler, as well as funding from AFOSR and ONR.

Lastly, I would like to thank my labmates and friends from graduate school for years of stimulating conversations in the countless hours and dollars spent at the coffee cart. Special acknowledgement to: Physics House, Chiefs10-40, Chain Rule, movie night (RIP), Shane Waterman (RIP), the undergrad who wrote Char Khadib on my evaluation form, and all iterations of '_____ghile' established throughout the years.

Chapter 2, in full, is a reprint of material as it appears in O. Khatib, B. Lee, J. D. Yuen, Z. Q. Li, M. Di Ventra, A. J. Heeger, V. Podzorov, D. N, Basov, "Infrared signatures of high carrier densities induced in semiconducting poly (3-hexylthiophene) by fluorinated organosilane molecules," Journal of Applied Physics, 107, 123702 (2010). The dissertation author was the primary investigator and author of this publication.

Chapter 3, in full, is a reprint of material as it appears in O. Khatib, J. D. Yuen, J. Wilson, R. Kumar, M. Di Ventra, A. J. Heeger, D. N. Basov, 'Infrared

spectroscopy of narrow gap donor-acceptor polymer-based ambipolar transistors,' Physical Review B 86, 195109 (2012). The dissertation author was the primary investigator and author of this publication.

Chapter 4, in part, has been submitted for publication of the material as it may appear in O. Khatib, A. S. Mueller, H. T. Stinson, J. D. Yuen, A. J. Heeger, D. N. Basov, "Electron and hole polaron accumulation in low bandgap ambipolar donor-acceptor polymer transistors imaged by infrared microscopy", to Physical Review B. The dissertation author was the primary investigator and author of this work.

Chapter 5, in full, is being prepared for publication of the material as it may appear in O. Khatib, J. D. Wood, A. S. McLeod, M. Goldflam, M. Wagner, J. W. Lyding, D. N. Basov, "Graphene-based platform for nano-scale infrared near-field nano-spectroscopy of biological substances in aqueous media". The dissertation author is the primary investigator and author of this work.

VITA

(2005)	Bachelor of Science in Physics, University of California, Irvine
(2005)	Bachelor of Science in Computer Engineering, University of California, Irvine
(2006-2007)	Graduate Teaching Assistant, University of California, San Diego
(2008)	Master of Science in Physics, University of California, San Diego
(2014)	Doctor of Philosophy in Physics, University of California, San Diego

PUBLICATIONS

O. Khatib, J. D. Wood, A. S. McLeod, M. Goldflam, M. Wagner, J. W. Lyding, D. N. Basov, "Graphene-based platform for nano-scale infrared near-field nano-spectroscopy of biological substances in aqueous media", in preparation.

M. K. Liu, B. C. Chapler, H. T. Stinson O. Khatib, D. J. Meyers, J. Chakhalian, D. N. Basov, "THz and near-infrared probe of the insulator-to-metal transition in $NdNiO_3$-based electric double-layer field effect devices", in preparation.

O. Khatib, A. S. Mueller, H. T. Stinson, J. D. Yuen, A. J. Heeger, D. N. Basov, "Electron and hole polaron accumulation in low bandgap ambipolar donor-acceptor polymer transistors imaged by infrared microscopy", submitted to Physical Review B.

M. D. Goldflam, T. Driscoll, D. Barnas, O. Khatib, M. Royal, N. Marie Jokerst, D. R. Smith, Bong-Jun Kim, Giwan Seo, Hyun-Tak Kim, D. N. Basov, "Two-dimensional reconfigurable gradient index memory metasurface", Applied Physics Letters 102, 224103 (2013).

O. Khatib, J. D. Yuen, J. Wilson, R. Kumar, M. Di Ventra, A. J. Heeger, D. N. Basov, "Infrared spectroscopy of narrow gap donor-acceptor polymer-based ambipolar transistors", Physical Review B 86, 195109 (2012).

J. W. Simonson, K. Post, C. Marques, G. Smith, O. Khatib, D.N. Basov, M. C. Aronson, "Gap states in insulating $LaMnPO_{1-x}F_x$ (x=0-0.3)", Physical Review B 84, 165129 (2011).

M. D. Goldflam, T. Driscoll, B. Chapler, O. Khatib, N. Marie Jokerst, S. Palit, D. R. Smith, Bong-Jun Kim, Giwan Seo, Hyun-Tak Kim, M. Di Ventra, D. N. Basov, "Reconfigurable gradient index using VO_2 memory metamaterials", Applied Physics Letters 99, 044103 (2011).

O. Khatib, B. Lee, J. D. Yuen, Z. Q. Li, M. Di Ventra, A. J. Heeger, V. Podzorov, D. N, Basov, "Infrared signatures of high carrier densities induced in semiconducting poly (3-hexylthiophene) by fluorinated organosilane molecules", Journal of Applied Physics 107, 123702 (2010).

D. Kingrey, O. Khatib, P. G. Collins, "Electronic fluctuations in nanotube circuits and their sensitivity to gases and liquids", Nano Letters 6, 1564 (2006).

ABSTRACT OF THE DISSERTATION

Infrared micro- and nano-spectroscopy of carbon-based materials

by

Omar Khatib

Doctor of Philosophy in Physics

University of California, San Diego, 2014

Professor Dimitri N. Basov, Chair

The following dissertation explores the low-energy physics and infrared properties associated with a suite of organic and molecular materials. The majority of the work is centered around organic semiconductors, specifically conducting polymers. First, we introduce a novel method of charge injection in organic semiconductors by exposure to vapors of fluorinated organosilane molecules. We show that ultra-high carrier densities in the range 10^{14} cm^{-2} are attainable, a regime that is inaccessable by conventional oxide-based electrostatic field-effect. Further, we provide spectroscopic evidence of delocalized states and thus metallic transport, signaling that such highly-doped polymer films are at the threshold of the metal-insulator transition, an area of both high academic and practical interest. The next two sections detail our investigation of a new class of narrow bandgap

donor-acceptor (DA) copolymers, based on benzobisthiadiazole (BBT) and diketopyrrolopyrrole (DPP), that demonstrate intrinsic ambipolarity when integrated in field-effect transistors. We perform a systematic infrared investigation of thin film transistors based on DA copolymers. We study the electronic excitations under both positive and negative gate biases, to determine the electron- and hole-induced IR spectral features. For high-mobility polymer films based on DPP, we observe distinct polaronic absorption features associated with both injected electrons and holes. We employ a customized diffraction-limited IR microscope to study the evolution of the electronic response throughout the channel of a functional field-effect transistor device. From the strength of the IR absorptions, we are able to generate a spatial map of the carrier density across the conduction channel. When biased at moderate gate biases in the 'ambipolar regime' where electrons and holes coexist in the channel, we register the transition from electron-polaron to hole-polaron IR absorption as a function of position. The last section introduces an entirely new concept in the field of near-field infrared nano-optics involving characterizing biological substances in aqueous media. We utilize a novel graphene-based liquid cell to trap biomolecules surrounded by water. We perform IR nano-imaging and nano-spectroscopy measurements on tobacco mosaic virus (TMV) aggregates in a graphene liquid cell. This work sets the stage for a new class of nano-scale experiments on molecular and biological systems.

Chapter 1

Introduction

Infrared (IR) and optical spectroscopy is universally recognized as an effective probe of vibrational and electronic properties of matter. Existing between microwave and ultraviolet radiation, and spanning the energy range from 2 meV to 6 eV, IR and optical light have direct access to important physical processes for virtually all materials. By spectrally monitoring the low-energy excitations of a system while tuning parameters such as temperature, doping (ie carrier density), or chemical composition, fundamental electromagnetic phenomena can be explored in a very wide phase space.

The sub-field of condensed matter physics consisting of organic, biological, and other soft materials (generously lumped together as 'carbon-based materials' in the dissertation title) presents a new set of challenges that have undergone considerably less investigation compared to conventional inorganic semiconducting and metallic systems. The following four chapters are work done to address several of these challenges, in an attempt to push the current boundaries of science ever further. The ubiquity of IR spectroscopy as an experimental tool ensures application over a number of length scales, from macroscopic crystals down to individual biomolecules. Through significant advances in measurement techniques, IR probes have found utility both in diffraction-limited and sub-diffractional experimental settings. As if by happenstance, the work presented here progresses in such a manner, from the macro- to the micro- to the nano-scale.

1.1 Organic semiconductors

1.1.1 High carrier densities in conjugated polymers

By virtue of being characterized as 'molecular' systems, polymers, organic crystals, and other van der Waals materials exhibit electronic phenomena typically confined to just a few unit cells. The weak van der Waals interaction results in extremely narrow energy bands in the solid state, and electron states that are very sensitive to the local morphology, disorder, and vibrational degrees of freedom. Thus, the science of organic semiconductors is driven by a cooperative effort from physicists, chemists, and material scientists.

Polymers, instrinsically insulating, are quasi-1D systems characterized by large energy gaps and low electrical conductivity. Charges tend to be localized on host atoms, hopping from site to site with a large effective mass. The conductivity can be increased by the continued addition of excess charges to the polymer chain in several ways. The discovery and development of conducting polymers in the late 1970s by chemical doping led to the Nobel Prize in Chemistry, awarded in 2000 to Heeger, MacDiarmid, and Shirakawa.

Due to the complexity of the energetic competition between externally applied fields, local morphological, and thermal disorder, there still does not exist a universal model of charge injection and transport in organic semiconductors. Thus, despite substantial progress in the field of organic electronics, there still remains a challenge to achieve a comprehensive understanding of charge carrier dynamics. This is especially true at higher carrier densities, a regime of both fundamental and practical interest for applications. In addition to conventional chemical doping, which is typically performed in solution, excess charge can be added via electric field-effect. Employing organic semiconductors as the active material in a field-effect transistor has become the benchmark system by which to study charged excitations in conjugated polymers. However both of these methods are limited in the extent of their doping efficiency. Chemical doping eventually results in a breakdown of the polymer backbone structure, while oxide-based transistors are limited by leakage currents and dielectric breakdown to modest carrier densities.

The use of fluorinated trichlorosilanes (FTS) has recently been introduced as a viable means to achieve high carrier densities in both organic molecular crystals and polythiophenes. In Chapter 2 we carry out the first spectroscopic investigation of FTS-modified films of a prototypical high-mobility polymer, poly(3-hexylthiophene) (P3HT). We report on the spectroscopic signatures of a high density of charges in a P3HT film introduced both through gating and FTS-doping. Capitalizing on model-independent sum rules for optical constants, we are able to extract carrier densities from absorption data for FTS-doped P3HT films. We observe a significant increase in the maximum attainable carrier densities in FTS-altered films compared to gating in an organic field effect transistor (OFET) architecture. We discuss this exciting result in the context of a critical assessment of carrier densities in OFETs employing both SiO_2 dielectric and high-κ dielectric constant oxides. Our work demonstrates that FTS doping offers an opportunity to study the rich physics near the insulator-to-metal transition of polymer semiconductors.

1.1.2 Donor-acceptor narrow gap ambipolar copolymers

Donor-acceptor (DA) copolymers experienced a flurry in activity in the early 1980s in an attempt to understand and control the energy bandgap, with the goal of achieving a zero-gap room temperature metal. A modern resurgence in utilizing the DA approach has resulted in the synthesis of ambipolar polymers, which until recently have not been available. The inherent chemical tunability afforded by the choice of donor and acceptor units has led to the realization of copolymers with very high mobility and extremely narrow bandgaps, responsible for the intrinsic ambipolarity. Significant improvements in these key areas are of both fundamental and practical interest for charge transport and light-emitting applications.

In Chapters 3 and 4 we report for the first time on ambipolar charge injection in narrow-gap polymers using infrared spectroscopy. New generations of DA copolymers based on benzobisthiadiazole (BBT) and diketopyrrolopyrrole (DPP) possess extremely small bandgaps below 1 eV. Further, DA systems incorporat-

ing DPP regularly yield field-effect mobilities exceeding 1 $cm^2v^{-1}s^{-1}$. Utilizing infrared methods, we are able to obtain a detailed characterization of the polymer band edge, and its behavior upon electrostatic doping of both holes and electrons. Our spectroscopic probe has access to the electronic excited states as well as IR signatures of injected charges in devices based on conventional silicon substrates. In addition to sharp mid-IR resonances associated with charge injection, we find a significant modification of the polymer band edge with doping. This work is the first systematic IR investigation of such a low bandgap ambipolar polymer system.

In our results for BBT-based polymers in Chapter 3, we find evidence of a polymer with a significant self-doping of holes. We did not find IR absorption features associated explicitly with mobile electrons, contrary to transport measurements. This discrepancy is discussed in Chapter 4, where we perform a combined transport and spectroscopic investigation on a high mobility polymer based on both BBT and DPP. In polydiketopyrrolopyrrole-benzobisthiadiazole (PDPPBBT) we register distinct IR resonances associated with electron and hole polaron absortion. We clarify the role and origin of charge trapping on electron transport, and its manifestation in the IR spectra.

1.1.3 Diffraction-limited IR microscopy as a comprehensive experimental probe

In Chapter 4, we perform a more detailed study of the spectroscopic signatures of both electron and hole injection in DA polymer FETs based on PDPPBBT using a diffraction-limited infrared microscope. Using IR microscopy, we are able to register distinct absorption associated with both electrons and holes, and provide a spatio-spectral map of the IR response throughout the conduction channel of an operating FET device. Further, based on the strength of the spectral features we are able to image the carrier density in the channel of an ambipolar DA polymer. We show that for certain voltage configurations, there is a coexistence of electrons and holes in the transistor channel. Our work provides a platform for combined transport and infrared studies of organic semiconductors on micron length scales relevant to functional devices.

1.2 Scattering scanning near-field optical microscopy (s-SNOM)

In biological and life sciences, infrared spectroscopy serves as a noninvasive probe of vibrational fingerprints used to identify chemical and molecular species, and can be used to characterize cells and tissues linked to specific diseases such as Alzheimer's. However, significant limitations of common implementations of IR spectroscopy include: i) the coarse spatial resolution (3 - 20 μm), restricted by diffraction and the long wavelength of IR light; ii) presence of multiple substances in heterogeneous biological specimens, thus leading to mixed results when the diffraction-limited areas are interrogated; and iii) incapability of measurements in aqueous media, due to the extremely strong IR absorption from water alone.

Recent advances in IR techniques have circumvented the diffraction limit by combining the use of an atomic force microscope (AFM) and IR lasers that illuminate the scanning tip. In scattering scanning near-field optical microscopy (s-SNOM), by analyzing the back-scattered light resulting from a tip-sample interaction (near-field), information can be gleaned at infrared frequencies with a spatial resolution no longer limited by the wavelength of light, but by the radius of the AFM tip apex (as small as 5-10nm).

1.2.1 Graphene-based liquid cells

Despite significant advances and widespread applications of 'apertureless' near-field spectroscopy, the research area of biological materials has thus far remained elusive. Physiological conditions required for experimentation are incompatible with a usual implementation of s-SNOM. In Chapter 5, we detail an innovative approach enabling nano-scale IR measurements to be performed on samples in a liquid environment. This experimental configuration utilizes graphene, a two-dimensional sheet of carbon atoms arranged in a honeycomb lattice that has remarkable mechanical, electrical, and IR properties.

In Chapter 5, we employ large area graphene, grown by chemical vapor deposition (CVD), as a monolayer lid over biomolecules trapped with water.

Graphene is impenetrable by gases and liquids, but is transparent for IR light enabling spectroscopy of substances underneath the membrane. We present IR nano-imaging and nano-spectroscopy data on TMV aggregates trapped with water in such a graphene liquid cell. These measurements are truly the first of their kind. We are able to resolve individual viruses through the graphene overlayer, and observe significant phase contrast in near-field nano-IR imaging experiments. Further we are able to register the amide I and II bands of TMV using IR nano-spectroscopy with a coherent broadband laser source. This work opens up a new class of experiments using scattering-based IR techniques to study biological systems in aqueous media.

Chapter 2

Ultra high carrier densities induced in organic semiconductors

We report on infrared (IR) absorption and dc electrical measurements of thin films of poly(3-hexylthiophene) (P3HT) that have been modified by a fluoroalkyl trichlorosilane (FTS). Spectra for FTS-treated films were compared to data for electrostatically-doped P3HT in an organic field-effect transistor (OFET). The appearance of a prominent polaron band in mid-IR absorption data for FTS-treated P3HT supports the assertion of hole doping via a charge-transfer process between FTS molecules and P3HT. In highly-doped films with a significantly enhanced polaron band, we find a monotonic Drude-like absorption in the far-IR, signifying delocalized states. Utilizing a simple capacitor model of an OFET, we extracted a carrier density for FTS-treated P3HT from the spectroscopic data. With carrier densities reaching 10^{14} holes cm^{-2}, our results demonstrate that FTS doping provides a unique way to study the metal-insulator transition in polythiophenes.

2.1 Introduction

Conjugated polymers, and specifically polythiophenes, are attractive materials for low-cost, large area, flexible electronics applications because of their

solution processability, superior film-forming properties, and comparatively high mobilities.[1,2,3,4] Because these systems are insulators with a moderate band gap, it is necessary to introduce mobile charges through doping or electric field gating, in order to initiate electrical transport. The quest to achieve a comprehensive understanding of charge carrier dynamics in the polymer host also requires extending the carrier densities toward the boundary of the insulator-to-metal transition (IMT). The IMT region is of fundamental interest as well, as some of the most fascinating electronic and magnetic many-body effects occur when both organic and inorganic insulators are driven towards the metallic state by photoexcitation, gating, or doping.[5,6,7]

To go beyond the charge density limits of conventional organic field-effect transistors (OFETs) with oxide insulators (roughly 10^{13} cm^{-2}), alternative methods have been introduced, including OFETs employing polymer electrolyte gating,[8,9,10,11,12] and the use of fluorinated organosilane molecules (known to self-assemble on surfaces) to chemically oxidize and thereby dope the organic semiconductor.[13,14] In this work, we explore the latter approach by modifying the electronic properties of the polymer poly(3-hexylthiophene) (P3HT) using fluorinated organosilanes. The organosilane molecules incorporate into the polythiophene structure, hydrolyze, and partially cross-link, forming a network that induces a strong p-type doping of P3HT.[13] The particular organosilane used in this work is (Tridecafluoro-1,1,2,2-tetrahydrooctyl)trichlorosilane ($C_8H_4F_{13}SiCl_3$), or simply fluoroalkyl trichlorosilane (FTS).

We have utilized infrared (IR) spectroscopy: a tool ideally suited for investigating fundamental electronic processes in organic semiconductors.[15] IR measurements directly probe electronic excitations associated with injected charges, and are complementary to transport measurements. With IR spectroscopy, we are able to characterize the low-energy excitations induced in FTS-modified structures by comparing the IR absorption of FTS-treated films to that of the same polymer film electrostatically doped in an OFET. At the highest carrier densities, we have observed both Drude absorption (indicative of delocalized states in a metal) and a broad mid-IR absorption (indicative of self-localized polaron states). We there-

fore demonstrate that FTS modification is a useful technique for exploring and exploiting the onset of metallic transport in polymers.

2.2 Experimental details

All IR and DC transport measurements reported here have been performed at room temperature using two types of devices: (a) two-terminal structures and (b) three terminal OFETs, shown in the insets of Figures 2.1 and 2.2, respectively. Two-terminal devices were fabricated by spin-coating a 10 - 15 nm-thick P3HT film onto an intrinsic H-terminated Si(111) substrate with bulk resistivity 30 $k\Omega\cdot$ cm, or onto a glass slide. Graphite contacts were painted on top of the polymer film, separated by 0.5 - 1 cm (Fig. 2.1 inset). Three-terminal P3HT-based OFETs were prepared by depositing thin (4 - 6 nm) film of P3HT on SiO_2/n-Si substrates (inset in bottom panel of Fig. 2.2). In the OFETs, 200 nm-thick SiO_2 on n-Si wafers were used, with the doping level suitable for IR transmission measurements. Gold source and drain electrodes were patterned on top of SiO_2 and spaced roughly 200 microns apart as previously described in Ref. (16).

IR measurements were performed ex-situ, i.e. after the P3HT samples have been brought to a highly conducting state by exposure to FTS. IR transmission measurements with a spectral resolution of 8 cm^{-1} were carried out in the mid-IR range (400 - 7000 cm^{-1}) and were extended to the far-IR region (down to 40 cm^{-1}) for selected structures. We employed a home-built IR microscope with the focus size reduced down to $d = 200$ μm, allowing us to explore the uniformity of electronic properties along the sample surface. Typically we recorded transmission spectra of an FTS-treated polymer, $T_{tr}(\omega)$, normalized by the transmission of a pristine sample, $T_p(\omega)$, on the same substrate. It is customary to plot these data in the form of the change in absorption ($\Delta\alpha$d) defined as:

$$\Delta\alpha d = 1 - T_{tr}(\omega)/T_p(\omega)). \tag{2.1}$$

For the OFETs we characterized transmission, $T(V_{gs})$, at various gate voltages, V_{gs}, and normalized these data by $T(V_{gs} = 0V)$. OFET data are presented

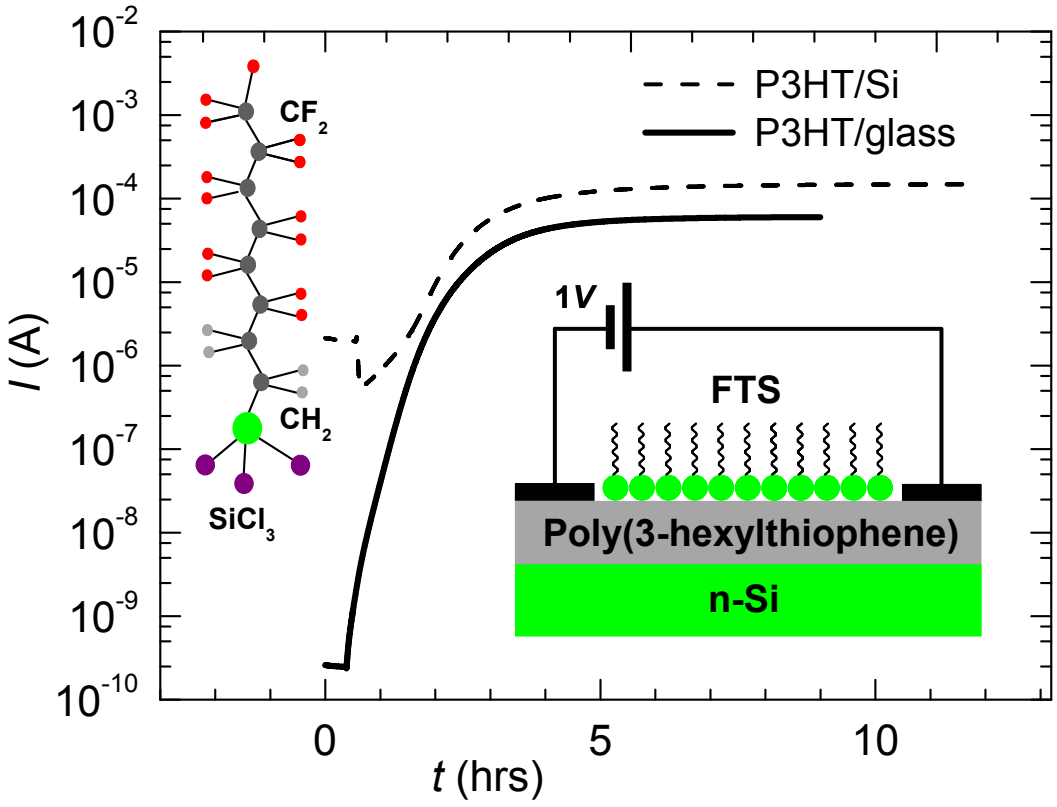

Figure 2.1: DC current flowing through a 10-15 nm-thick P3HT film exposed to the fumes of (tridecafluoro-1,1,2,2-tetrahydrooctyl)-trichlorosilane (FTS) as a function of exposure time. Dashed line: P3HT on a semi insulating (transparent for IR) Si(111) substrate. Solid line: P3HT on a glass substrate. Measurements are performed with V= $1V$ applied between graphite contacts that define a 1 x 1 cm^2 P3HT film. The left inset shows the structure of FTS molecules. The right inset shows a conceptual geometry of 2-probe samples. The apparent large background conductivity in the P3HT/Si device is due to the residual bulk conduction through the Si substrate.

as:

$$\Delta\alpha d = 1 - T(V_{gs})/T(V_{gs} = 0V), \tag{2.2}$$

where d is the thickness of the accumulation layer (typically 1 - 2 nm) and $T(V_{gs} = 0V)$ corresponds to the transmission at zero V_{gs}.

2.3 Results

2.3.1 DC transport data

Figure 2.1 shows DC transport data for a P3HT film obtained during exposure to FTS vapor. A dramatic increase of the DC current, by 5 - 6 orders of magnitude, is observed within the first few hours of the treatment. The large background conductivity of P3HT/Si(111) samples before the FTS exposure (dashed line) is due to the shunt by the 30 kΩ·cm substrate. The magnitude of the current in the saturated regime is similar for both P3HT/Si(111) and P3HT/glass. The effect of FTS on conductivity is persistent: FTS-altered P3HT shows no degradation of the high-conductivity state, provided the samples are stored in high vacuum or in an atmosphere of dry non-polar gases. The conductivity lasts for weeks in ambient atmosphere albeit with some gradual degradation accelerated by humidity. FTS-induced modification of the DC conductivity is similar to results reported for FTS layers grown at the surface of organic molecular crystals.[14] For molecular crystals, the FTS is restricted to the surface of the crystal; since FTS molecules cannot penetrate the tightly packed molecular structure, they form a self-assembled monolayer at the surface.[14] In a polymer with weak interchain interactions, however, the entire volume of a 10 nm film reacts with FTS, evidenced by a change in the color of P3HT from purple to transparent as the result of FTS exposure.[13]

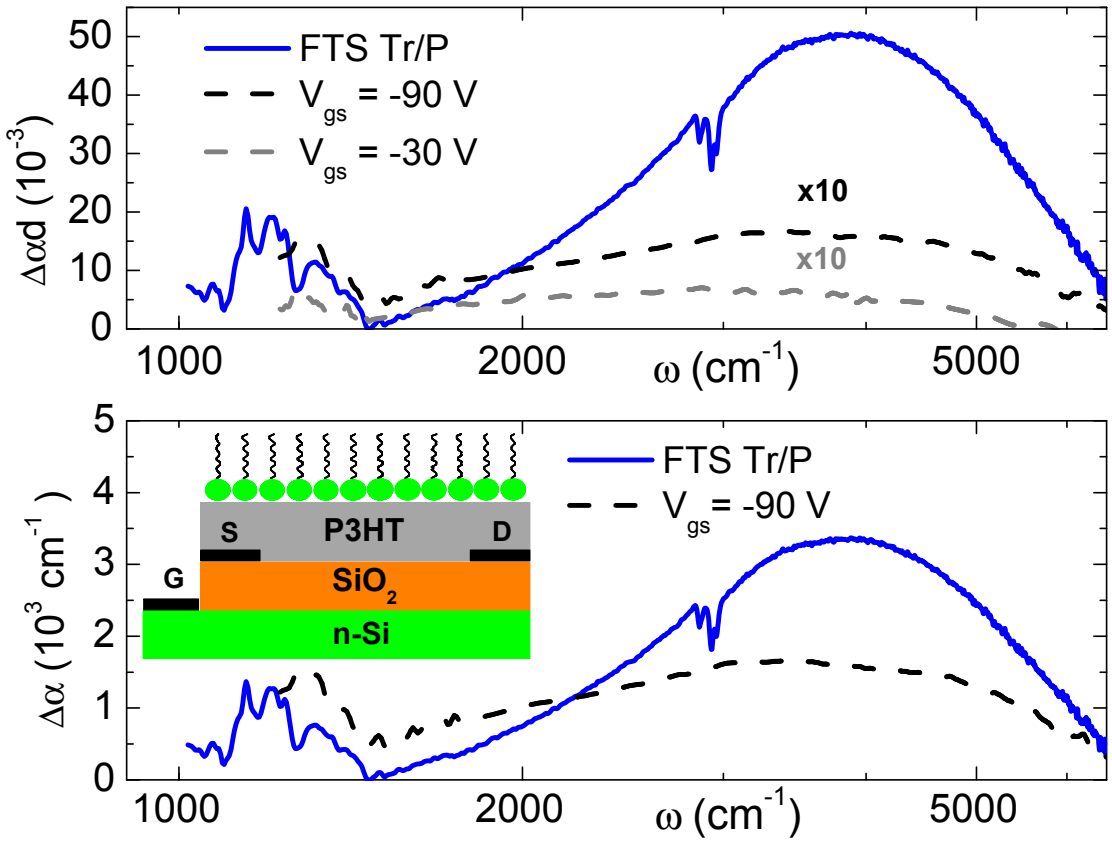

Figure 2.2: IR response of P3HT film modified by electrostatic doping in an OFET structure and under exposure to FTS fumes. Top panel: Mid-IR absorption $\Delta\alpha d = (1-T(V_{gs})/T(V_{gs} = 0V)$ for a device gated at $V_{gs} = -90V$ (black dashed curve) and $V_{gs} = -30V$ (gray dashed curve); $\Delta\alpha d = (1-T_{tr}/T_p)$ for FTS-modification with no applied bias (blue solid curve). Bottom panel: Change in the absorption coefficient $\Delta\alpha$ for the same device. Bottom inset: Schematic of FTS-treated OFET device.

2.3.2 IR Spectroscopy and comparison of FTS and electrostatic charge injection

The three-terminal OFETs (Fig. 2.2) offer known advantages for studying electronic effects in organic semiconductors,[17,16,18,19,20,21,22,23,24,25,26,27] and will serve as a reference system for characterizing the IR absorption associated with FTS effects on the electronic transport. We first injected charges in a P3HT film by applying a gate voltage, forming a hole-accumulation layer in the polymer at the interface with SiO_2. With this gate-induced carrier density, we observed the spectroscopic fingerprints of electrostatic charge injection (black and grey dashed lines in top panel of Fig. 2.2).[16] These include: (i) sharp peaks in the frequency range 1200 - 1400 cm^{-1} attributable to infrared active vibrational modes (IRAVs) and (ii) a broad band centered around 3500 cm^{-1} attributable to polaron absorption. The oscillator strength of these features, proportional to the area under $\Delta\alpha d$ spectra, is voltage-dependent in agreement with published data.[16]

After verifying the "fingerprint absorption" of the OFET, we subjected the same device to FTS fumes and repeated the measurements after 6 hours of exposure (blue line in top panel of Fig. 2.2). In both cases, we observed sharp resonances in the frequency range between 1000 - 1500 cm^{-1} and an absorption band centered at 4000 cm^{-1}. The low frequency structure is reminiscent of IRAVs seen in the OFET. The apparent agreement is improved further with OFETs employing TiO_2 as the gate insulator, as SiO_2 allows observation of only the higher energy IRAVs.[16]

Upon detailed investigation, however, we found that the FTS layer itself grown on various substrates (including KBr and SiO_2) exhibits absorption resonances in the same frequency range as the electrostatically-induced IRAVs in P3HT (inset in Fig. 2.3). Here we compare the absorption of P3HT two-terminal device subjected to FTS fumes to that of FTS-coated KBr. Note that clean KBr substrates are transparent in the mid-IR, and since FTS does not induce any measureable DC conductivity in KBr, we conclude that these peaks are primarily formed by the intrinsic vibrational modes of an FTS self-assembled network. The two largest peaks are most likely due to the six CF_2 groups in each molecule, which typically have stretching frequencies in this range.[28,29,30]

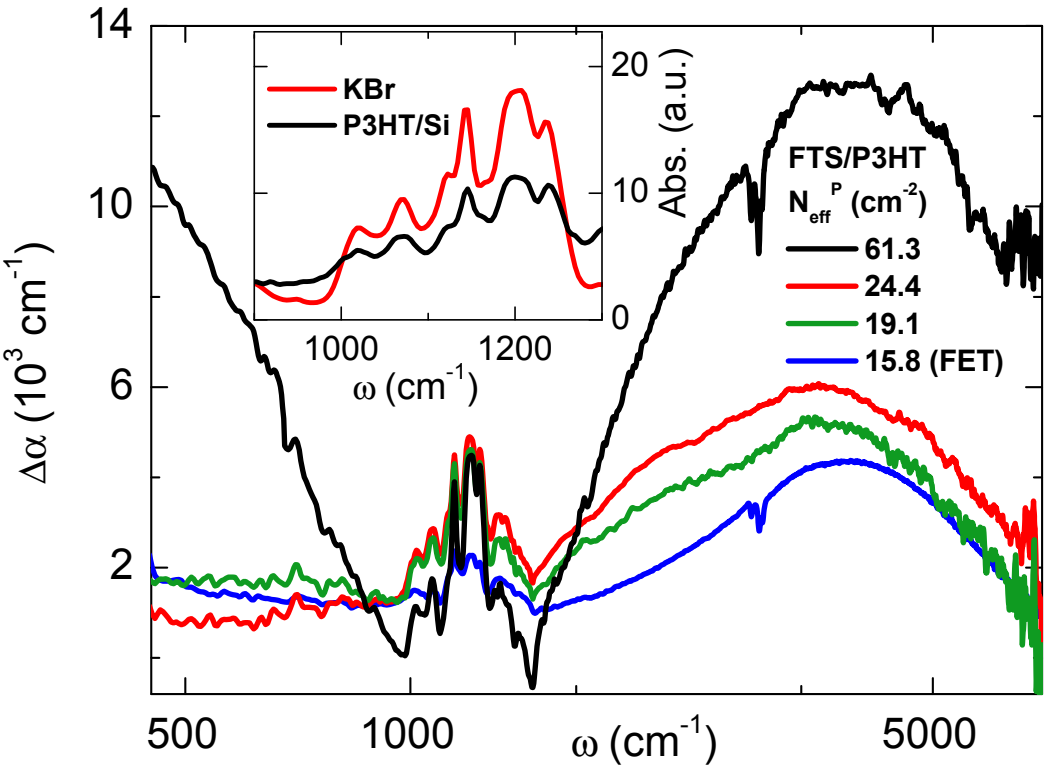

Figure 2.3: IR absorption of four different P3HT-based structures extended down to 40 cm^{-1} to include the far-IR range of the spectrum. The blue curve is FTS-induced absorption of the FET device presented in Figure 2.2. All other curves are 2-probe (ungated) P3HT/Si structures doped with FTS. The curves are labeled according to their integrated polaron spectral weight (detailed in text) and listed in order of polaron absorption strength. Inset: Vibrational spectrum of an FTS-treated P3HT/Si sample and FTS-coated KBr substrate.

The broad absorption band at higher frequencies (centered at 4000 cm^{-1}) in the IR spectra of both the gated P3HT devices and P3HT altered by FTS in Figure 2.2 arises from optical transitions to energy levels within the energy gap. In nondegenerate ground-state polymers, excess charges lead to the formation of either polaron or bipolaron states within the gap. This absorption from the localized polaron states is a characteristic spectral feature of charge injection in polymers. The distinction between polarons and bipolarons in the context of FTS-doping will be discussed in the next section, and the broad absorption will be referred to as a "polaron band"for simplicity. Similar polaron bands are also observed in photoexcited and chemically-doped polymers, and their line shape can be quantitatively described by models of polaron absorption.[31,32,1,33,34,35,36] The appearance of the prominent polaron band in the FTS-induced absorption in the OFET provides evidence of oxidation or p-type doping in the polymer host. In control experiments, we exposed KBr, Si, and GaAs substrates to FTS vapors. We did not find any significant modification of the absorption in the range where FTS-altered P3HT displays a polaron band. Although the polaron bands and IRAV resonances appear simultaneously in IR spectra for electrostatically and/or chemically doped polymers,[16,18,37,1,33,36] the contributions from direct absorption of the FTS network discussed above do not allow unambiguous identification of IRAV features of FTS-controlled P3HT.

We now analyze the strength of absorption of the gate-induced and FTS-induced polaron band in the P3HT film, both produced in the same OFET device. It is customary to define an effective spectral weight

$$N_{eff}^{P} = \int_{Pol} (\Delta\alpha d) d\omega, \tag{2.3}$$

where the integration is done over the polaron band. According to the oscillator strength sum rule,[38] this spectral weight is proportional to the density of charges participating in an absorption feature: a polaron band in this case. The $\Delta\alpha$d spectra plotted in Figure 2.2 reveal that FTS-induced absorption is an order of magnitude stronger compared to that of the OFET device under $V_{gs} = -90V$. This enhancement is at least in part due to the bulk nature of the doping in the

P3HT film caused by the reaction with FTS. Doping throughout the thickness of the film results in a larger net absorption than that obtained from gating the same OFET (gate-induced charges are confined within a 1 - 2 nm thick accumulation layer). The bottom panel in Figure 2.2 compares only the change in the absorption coefficient, $\Delta\alpha$. After properly correcting for the difference in thicknesses of the respective layers, it is apparent that the FTS reaction still yields higher doping levels than obtained by applying the highest sustainable gate voltage (blue and black curves in lower panel of Fig. 2.2).

2.3.3 FTS-treated P3HT

Figure 2.3 shows IR absorption spectra for three different P3HT/Si two terminal structures and a P3HT OFET obtained in separate FTS treatments. The polaron band is reproduced in all spectra, reaffirming the assertion that this spectroscopic feature arises from doping by reaction with FTS. The oscillator strength of the polaron feature varies for different FTS treatment experiments, and can even vary across the same sample. The energy of the polaron absorption reflects the degree of order between polymer chains[36] and therefore can be expected to show some sample-to-sample variation. As shown in Figure 2.3, we do find minor nonsystematic variation of the frequency of the polaron peak. Figure 2.4 shows data obtained by probing several different spots (separated by 1 mm) on the same two-terminal P3HT/Si sample. 1 mm is an enormous length scale compared to that of the features seen in AFM images of FTS-treated films,[13] calling for further studies with nano-scale spatial resolution that are now possible.

Structures which showed the most intense polaron band oscillator strengths reveal an additional feature in the far-IR absorption (black trace in Fig. 2.3, Fig. 2.4). The monotonic increase of this far-IR absorption towards lower frequencies (for $\omega < 1000$ cm^{-1}) is the Drude-like response of delocalized charge carriers,[38] and apparently signifies metallic transport in FTS-doped films. The low-energy absorption persists at low temperatures, consistent with the notion of metallic transport, with a modified ω-dependence to be reported in a separate publication. From the data in Fig. 2.4, we extract a two-dimensional (2D) conductivity of

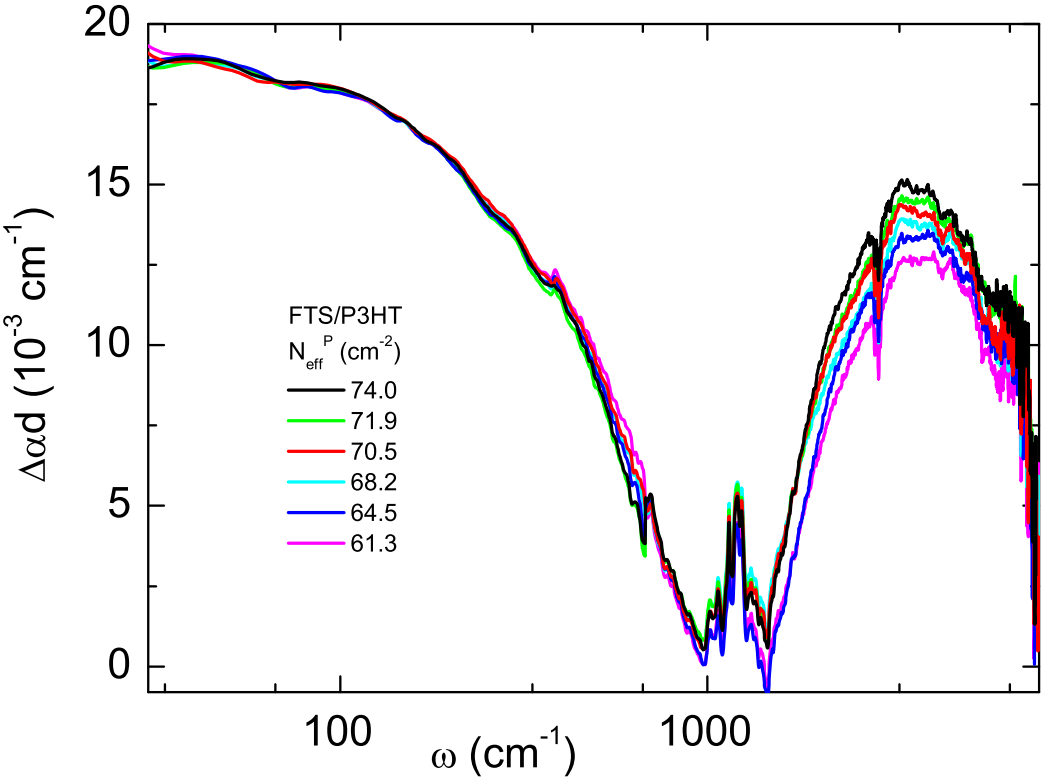

Figure 2.4: IR absorption spectra collected from different spots on a single $1x1$ cm^2 P3HT/Si sample doped with FTS to saturation. Probed locations are separated by 1 mm

σ_{DC}^{2D} =.970 $k\Omega^{-1}$, which is consistent with the highest values seen in transport.[13] The coexistence of metallic (delocalized) and polaronic (localized) states may point to a phase-separated system.

Additionally from Fig. 2.4, the Drude absorption appears to be more uniform over the large length scale considered. This suggests that the variation in the mid-IR absorption is likely due to light scattering, as opposed to inhomogeneities in the FTS treatment. Some inevitable swelling occurs in doped films, altering the surface morphology and leading to a reduced IR signal through regions with large surface irregularities. IR microscopy at the nano-scale is necessary to resolve such issues of inhomogeneity.[39]

2.4 Analysis and discussion

2.4.1 Quantifying carrier density from IR data

The gate-induced or doping-induced carrier density in P3HT can be extracted from the spectroscopic data. Note that an OFET can be modeled as a parallel plate capacitor in which the charge density N_{2D} is proportional to the applied gate voltage:

$$N_{2D} = \frac{\kappa\epsilon_0}{eL} V_{gs}, \tag{2.4}$$

where κ and L are the dielectric constant and thickness of the gate insulator, respectively. Naturally, N_{2D} is the same at both interfaces of the dielectric (i.e., in the gate electrode and in the OFET accumulation layer). The 2D carrier density in an accumulation layer in the P3HT-based OFET can thus be obtained directly from the applied gate voltage. Using the effective spectral weight N_{eff}^{P} defined earlier (Eqn. 2.3), there exists a one-to-one correspondance between the carrier density and the strength of the polaron absorption. The validity of this approach is confirmed by the linear dependence of N_{eff}^{P} on V_{gs} observed in OFETs with SiO_2 insulator (red triangles in Fig. 2.5). Previous work on SiO_2-based P3HT OFETs has shown a 2D carrier density reaching 10^{13} holes cm^{-2} at $V_{gs} = -100V$

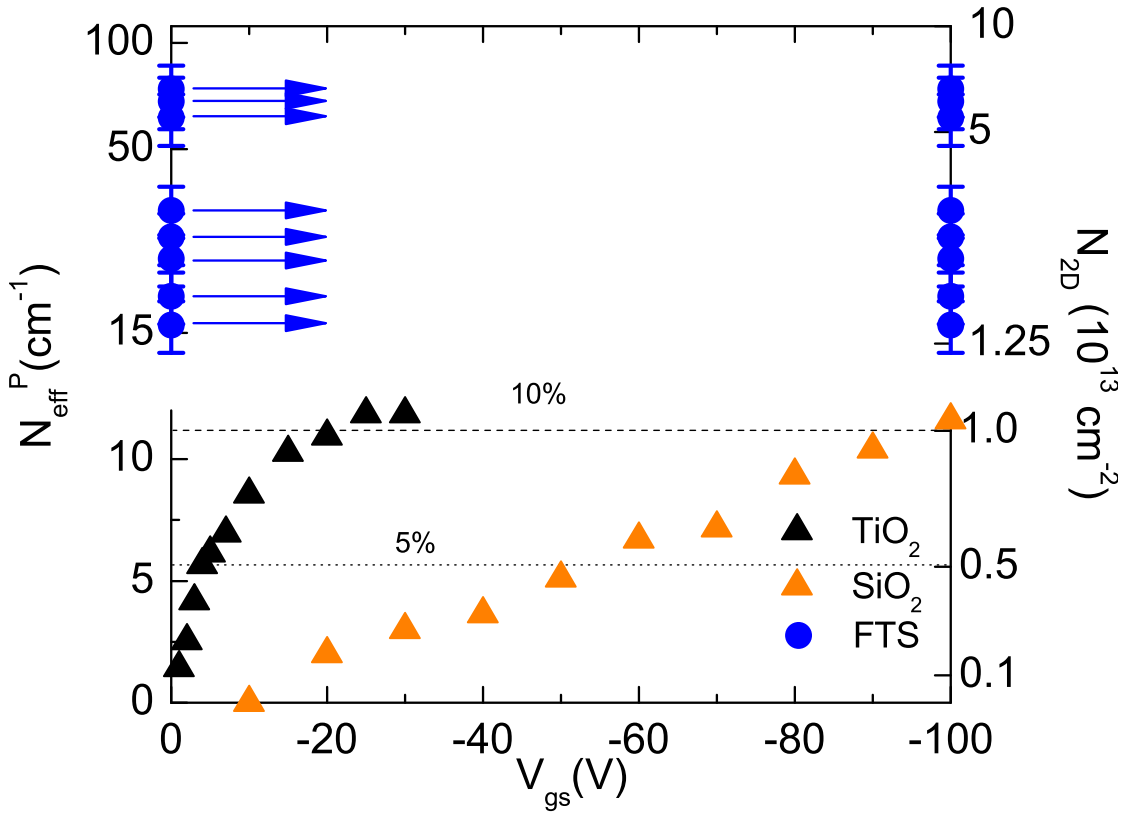

Figure 2.5: Effective 2D spectral weight of the polaron band N_{eff}^{P} and corresponding 2D carrier density plotted as a function of the applied gate voltage for SiO_2 ($|V_{gs}|$=0-100V) and TiO_2 ($|V_{gs}|$=0-30V)-based FET devices (triangles). The blue circles are N_{eff}^{P} and N_{2D} associated with the FTS-doped P3HT structures, with error bars due to the uncertainties in film thickness. Dotted and dashed lines indicate doping levels of 5% and 10%, respectively, for P3HT.

in structures with similar thickness of the gate insulator[18] and is limited by the break-down of the insulator.

The doping-induced carrier density in FTS-treated P3HT can then be obtained by integrating the absorption spectra:

$$N^{P}_{eff,FTS} = \int_{Pol} (\Delta\alpha) d\omega. \tag{2.5}$$

Figure 2.5 shows a comparison of for the OFET- and FTS-based methods of introducing charge carriers. It is evident from the plot that much higher carrier densities are attainable in FTS-doped P3HT, delivering as much as an order of magnitude enhancement over OFETs.

The capacitor model indicates that carrier densities in OFETs can in principle be increased with an appropriate choice of gate insulator. However, the experimental reality of OFETs employing high dielectric constant oxides as gate insulators is more complex than this simple conjecture. In Figure 2.5 we plot data for OFETs with TiO_2 ($\kappa = 37$) and SiO_2 ($\kappa = 3.9$),[16] and indeed devices employing TiO_2 dielectrics show strong enhancement of the carrier density (blue triangles), but only at small V_{gs} in the regime where the carrier density still varies linearly with the gate voltage. At V_{gs} approaching $-30V$ ideal OFET behavior is arrested due to high leakage current preempting breakdown at yet higher V_{gs}. In our experience, TiO_2 dielectrics yield no sizable improvement to the maximum possible carrier densities in OFETs compared to SiO_2-based devices. The data in Figure 2.5 reaffirm that FTS modification of polymers offers a viable means to achieve carrier densities significantly exceeding that of oxide-based OFETs. It is important to note that the FTS-induced carrier densities shown in Fig. 2.5 are calculated considering only the polaron band. Including the low-energy Drude absorption in the integral in Eqn. (2.5) puts the density of injected carriers from FTS molecules slightly higher in the 10^{14} holes cm^{-2} range for the highly-doped films.

2.4.2 Insulator-to-metal transition in P3HT

Data reported in Figs. 2.3 - 2.5 may reveal additional details about the insulator-metal transition that occurs in doped P3HT. In Ref. (18), three possible

theoretical scenarios were suggested to describe the IMT in P3HT: (i) a first-order transition between a bipolaron and a polaron lattice, (ii) a gap closure between the polaron band and the valence band, and (iii) a gap closure between the bipolaron band and the valence band. A schematic diagram of these three possibilities for a transition is displayed in Fig. 2.6. The critical doping concentration for both scenarios (i) and (iii) was predicted to be near 10%, or $\tilde{1}0^{13}$ cm^{-2}, while for scenario (ii) it is closer to 5%. It is evident from Fig. 2.5 that 10^{13} cm^{-2} is barely attainable in gated OFETs. Despite being on the cusp of the IMT, no signs of metallic conductivity are evident in the OFET absorption data at the highest gate voltages. Using a theoretical model originally proposed by Brazovskii and Kirova,[40] the lowest optical transition frequency was calculated to be 0.16 eV for polarons, and 0.45 eV for bipolarons.[18] With these energies in mind, P3HT OFET data show one broad absorption at 3500 cm^{-1} (0.44 eV) at all dopings up to 10%, indicating that this absorption is likely due to bipolarons. This suggests a merging of the valence and bipolaron band as the mechanism by which an IMT occurs.

Here, we have increased the carrier density in P3HT an order of magnitude further, with clear signs of metallicity, and both the peak structure and position of the mid-IR absorption band have not changed appreciably. Therefore, in light of the three IMT scenarios presented earlier, the new data would provide additional evidence for the physical picture of a bipolaron band merging with the valence band to form a partially-filled (metallic) energy band. Previous work on P3HT has led to numerous interpretations of the low-energy excitations in the absorption spectrum for the various methods of introducing excess charges (electrostatic, chemical, etc.).[18,31,36,41,42] To evaluate these interpretations as well as the models used to calculate polaron and bipolaron energies, effects such as disorder must be taken into account. This is especially true in the case of FTS doping, where the penetration of FTS molecules into the bulk of the P3HT film may have a significant effect on the local order of the polymer chains. Perhaps more importantly, most of the theoretical models used to calculate these energies assume non-interacting polarons. In order to completely capture all of the essential physics at such high carrier densities near the IMT, interactions between the polarons must be taken

into consideration.[43,44]

The previous interpretation of a continuous transition from an insulating to metallic state is based upon the assumption of a homogeneous film. This may not necessarily be the case. The coexistence of metallic and localized features in the IR absorption data (Figs. 2.3 and 2.4) for FTS-doped films is indicative of phase separation. Earlier, Dhoot et al. estimated that a small fraction ($\sim$ 1%) of the field-induced carriers in regio-regular P3HT OFETs occupy delocalized states at high carrier densities, while most charges remain in the lower-energy localized states.[23] Phase separation may be a common attribute among conducting polymers. Earlier work on heavily-doped polyacetylene has demonstrated metallic absorption appearing simultaneously with localized excitations (IRAVs). Recent work on polyaniline, however, has demonstrated a metallic response in reflectance simultaneously with reduced-strength IRAVs.[45] The strong absorption of FTS molecules obscures the IRAV spectrum in FTS-doped P3HT, but it is important to note that the metallic response observed in Fig. 2.3 occurs simultaneously with the highest polaron absorption, relative to other treated samples. Truly resolving these issues certainly requires these effects to be thoroughly studied at the nano-scale.

2.5 Conclusions

The IR data (Figs. 2.2, 2.3) confirm the assertion that the large increase in DC conductivity in FTS-treated structures is based on doping via electron transfer from the conjugated polymer to electronegative FTS molecules located nearby the polymer chains. The data in Figure 2.5 demonstrate that carrier densities in FTS-doped films are significantly higher than those in OFETs, with the highest values reaching nearly 10^{14} holes cm^{-2}. Such strong doping is indicated by the significantly enhanced polaron band and the strong far-infrared Drude-like absorption. The range of carrier densities is consistent with the variation seen in transport measurements of FTS-treated P3HT, which typically have saturated DC conductivities in the range $\sigma_{DC}^{2D} = 10^{-4}$ - 10^{-3} Ω^{-1}.[13] The Drude-like form

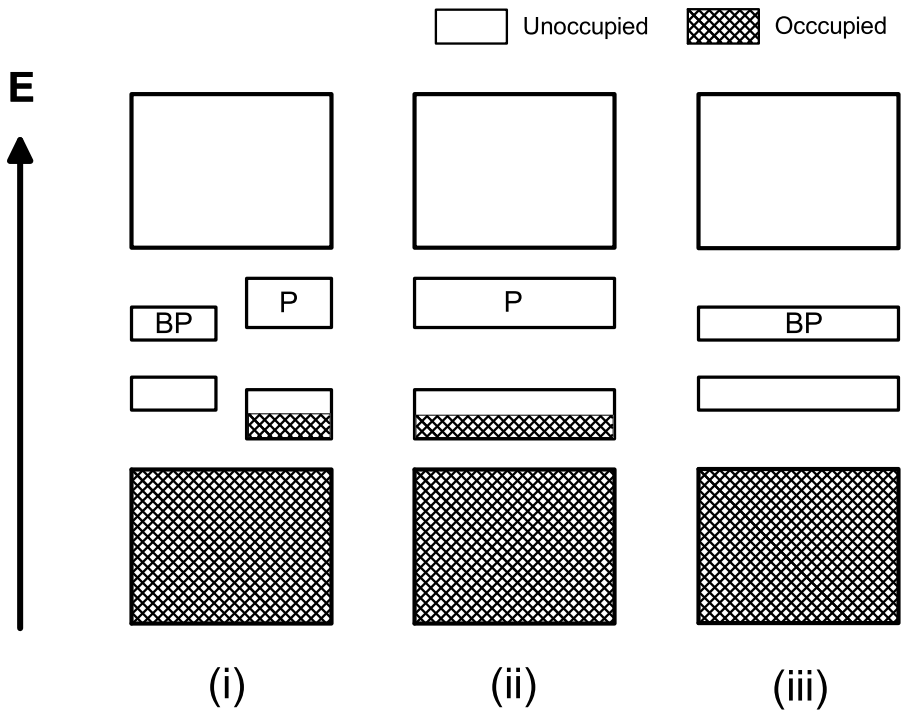

Figure 2.6: Schematic energy level diagram displaying three possible scenarios for an insulator-metal transition in P3HT upon doping: (i) a first-order transition from a bipolaron to a polaron lattice, leading to a partially-filled band; the (ii) polaron or (iii) bipolaron band broadens to merge with the valence band.

of the far-IR absorption is characteristic of a free carrier response. These data therefore indicate that FTS-controlled films can be doped to sufficiently high carrier densities (of order 10^{14} holes cm^{-2} or 10^{21} cm^{-3}) to be on the metallic side of the insulator-to-metal transition. The transition to the metallic state in this highly-doped regime is in accord with the analysis of required carrier densities.[18] With the number of carriers surpassing 10^{14} holes cm^{-2}, FTS-doping provides an opportunity to study the nature of the insulator-to-metal transition in conjugated polythiophenes. When combined with IR nanoscopy, these studies can directly address competing physical descriptions of the IMT, such as phase separation or a continuous transition to metallic states.

2.6 Acknowledgements

This work was supported by AFOSR Grant No. FA9550-09-1-0566 and University of California. Chapter 2, in full is a reprint of material as it appears in O. Khatib, B. Lee, J. D. Yuen, Z. Q. Li, M. Di Ventra, A. J. Heeger, V. Podzorov, D. N, Basov, "Infrared signatures of high carrier densities induced in semiconducting poly (3-hexylthiophene) by fluorinated organosilane molecules," Journal of Applied Physics, 107, 123702 (2010). The dissertation author was the primary investigator and author of this publication.

Chapter 3

Infrared spectroscopy of BBT-based narrow gap donor-acceptor copolymers

Donor-acceptor (D-A) copolymers have recently emerged as versatile materials for use in a large variety of device applications. Specifically, these systems possess extremely narrow bandgaps, enabling ambipolar charge transport when integrated in solution-processed organic field-effect transistors (OFETs). However, the fundamentals of electronic transport in this class of materials remain unexplored. We present a systematic investigation of ambipolar charge injection in narrow-gap D-A conjugated polymers polybenzobisthiadiazole-dithienopyrrole (PBBTPD) and polybenzobisthiadiazole-dithienocyclopentane (PBBTCD) using infrared (IR) spectroscopy. We observe a significant modification of the absorption edge in both PBBTPD- and PBBTCD-based OFETs under the applied electric field. The absorption edge reveals hardening under electron injection and softening under hole injection. Additionally, we register localized vibrational resonances associated with injected charges. Our findings indicate a significant self-doping of holes that is modified by charge injection. Observations of both electron and hole transport with relatively high carrier mobility strongly suggest an inhomogeneous, phase-separated conducting polymer.

3.1 Introduction

Organic semiconductors have emerged as attractive materials for use in a variety of large-area, low-cost electronic applications.[46,47] Recently, organic field-effect transistors (OFETs) based on solution-processed conjugated polymers have attained carrier mobilities exceeding 1 $cm^2V^{-1}s^{-1}$ for unipolar p-type[48] and n-type devices.[49] There is considerable interest in ambipolar polymers for use in organic complementary logic electronics similar to standard silicon CMOS technology.[50] One very efficient way to achieve intrinsic ambipolarity in conjugated polymers is through the use of donor-acceptor (DA) structures.[51,52,53] With appropriate choices for donor and acceptor moieties, electron and hole injection barriers can be minimized by effectively tuning the highest-occupied (HOMO) and lowest-unoccupied (LUMO) molecular orbitals of the DA polymer.[54,55,56] This inherent tunability has enabled fabrication of polymers with extremely narrow energy bandgaps, highlighting DA systems as useful materials for photovoltaic and light-emitting devices.[57] When incorporated in ambipolar OFETs, DA polymers allow for a detailed investigation into mechanisms of electrostatic injection of both electrons and holes into a polymer host. Very recently, a new class of DA polymers based on electron acceptor benzobisthiadiazole (BBT) have demonstrated ambipolar OFET operation with reasonably high carrier mobilities[58] between 10^{-2} - 10^{-1} $cm^2V^{-1}s^{-1}$. Additionally, these systems possess extremely narrow bandgaps below 1 eV, as well as many other unusual optical, electrochemical, and transistor properties.[53,58,59,60] Polymers with such small energy gaps alleviate large injection barrier issues that prevent a thorough study of both electron and hole doping in systems employing commonly used gold electrodes.

We present a systematic investigation of ambipolar charge injection in OFETs based on narrow-gap DA conjugated polymers polybenzobisthiadiazole-dithienopyrrole (PBBTPD) and polybenzobisthiadiazole-dithienocyclopentane (PBBTCD) using infrared (IR) spectroscopy. IR methods have the advantage of directly probing the electronic excitations associated with charge injection.[16,27,61,62] A detailed characterization of the ungated polymer absorption edge in the mid-IR is carried out using spectroscopic ellipsometry. We then

observed a significant modification of the absorption edge in both PBBTPD- and PBBTCD-based OFETs under the applied electric field. The absorption edge reveals hardening under electron injection and softening under hole injection. In addition to this field-induced behavior near the polymer band edge, we find evidence of localized charge carriers in the form of sharp vibrational resonances at lower energies. We critically assess the possible role of several physical mechanisms that can be responsible for these voltage-dependent features in the IR transmission data, including absorption due to charged molecular species (i.e. polarons).

3.2 Experimental

A detailed description of polymer synthesis and sample preparation for Poly[(4,7-bis(3-hexylthien-2-yl)-2λ4δ2-benzo[1,2-c;4,5-c′]bis[1,2,5]thiadiazole)-alt-(N-(3,4,5-tris(dodecyloxy) phenyl)-dithieno[3,2-b:2′,3′-d]pyrrole)] (PBBTPD) and Poly[(4,7-bis(3-hexylthien-2-yl)-2λ4δ2-benzo[1,2-c;4,5-c′]bis[1,2,5]thiadiazole)-alt-(3,3-bis(2-ethyl hexyl) 4H-cyclopenta[2,1-b:3,4-b′]dithiophene)] (PBBTCD) can be found in Ref. (58).

Partially transparent 20-30 Ω-cm n-doped Si wafers served as the back gate in devices employing two types of dielectrics: SiO_2 (ϵ= 3.9) and Ta_2O_5 (ϵ = 24). Electrodes were patterned using standard photolithography and were formed with e-beam evaporation of 3 nm of nickel followed by 47 nm of gold. Thin 25nm polymer films were spin-coated onto substrate surfaces treated with decyltrichlorosilane (DTS) to lower interfacial trap densities and improve device performance. In structures with Ta_2O_5 gate dielectric, a thin buffer layer of SiO_2 (10nm) is grown just below the polymer for deposition of DTS. Devices suitable for simultaneous electrical and spectroscopic characterization contained source and drain electrodes, while structures optimized for IR measurements, in order to obtain the highest possible quality optical data, contained a single terminal enclosing a 3 mm^2 area (inset in Fig. 2). Previous micro-spectroscopy studies have determined that the charge injection landscape in polymer OFETs with low leakage SiO_2 gate insulator remains uniform over cm length scales.[16]

Current-voltage IV characteristics of our OFETs with channel widths of 1 mm and channel lengths of 5 μm were obtained using a Keithley 4200 Semiconductor Parametric Analyzer and a Signotone Micromanipulator S-1160 probe station. Transient current measurements were performed by a Keithley 6487 picoammeter, using AC square wave pulses with a period of 10s for both electron and hole injection.

Infrared transmission data were acquired in vacuum using a Bruker Vertex 70v FT-IR spectrometer with a spectral resolution of 8 cm^{-1}. Broadband light from a thermal globar source was focused onto a liquid nitrogen-cooled HgCdTe (MCT) or InSb IR detector for mid-IR (750-6500 cm^{-1}) and near-IR (5000-10000 cm^{-1}) measurements, respectively. Raman spectra were obtained by a Bruker Senterra dispersive Raman microscope using an excitation laser of wavelength 532 nm. All electrical and optical measurements were performed at room temperature.

In order to obtain frequency-dependent optical constants of the studied polymers we performed variable angle spectroscopic ellipsometry (VASE) measurements on thin films spin-coated onto unpatterned substrates. Data were recorded using a commercial Woollam ellipsometer (IR-VASE) based on a Michselson interferometer (Bruker 66vs), covering the energy range 0.05 - 0.7 eV. The ellipsometric parameters Ψ and Δ, are related to the Fresnel reflection coefficients for p- and s-polarized light (R_p and R_s) through the equation $\frac{R_p}{R_s}$=tan(Ψ)$e^{i\Delta}$. The complex dielectric function of each polymer was modeled by considering a single Kramers-Kronig consistent Cody-Lorentz (C-L) oscillator[63] to fit the ellipsometric data. This model has been used to successfully describe optical absorption of a disordered semiconductor near the band edge.[64] Data for each polymer on SiO_2/Si at incidence angles of 60° and 75° were used for modeling.

3.3 Results

3.3.1 OFET transport data

The bottom panels in Figure 1 show typical output curves for OFETs based on small-gap polymers PBBTPD (Fig. 3.1a) and PBBTCD (Fig. 3.1b). The

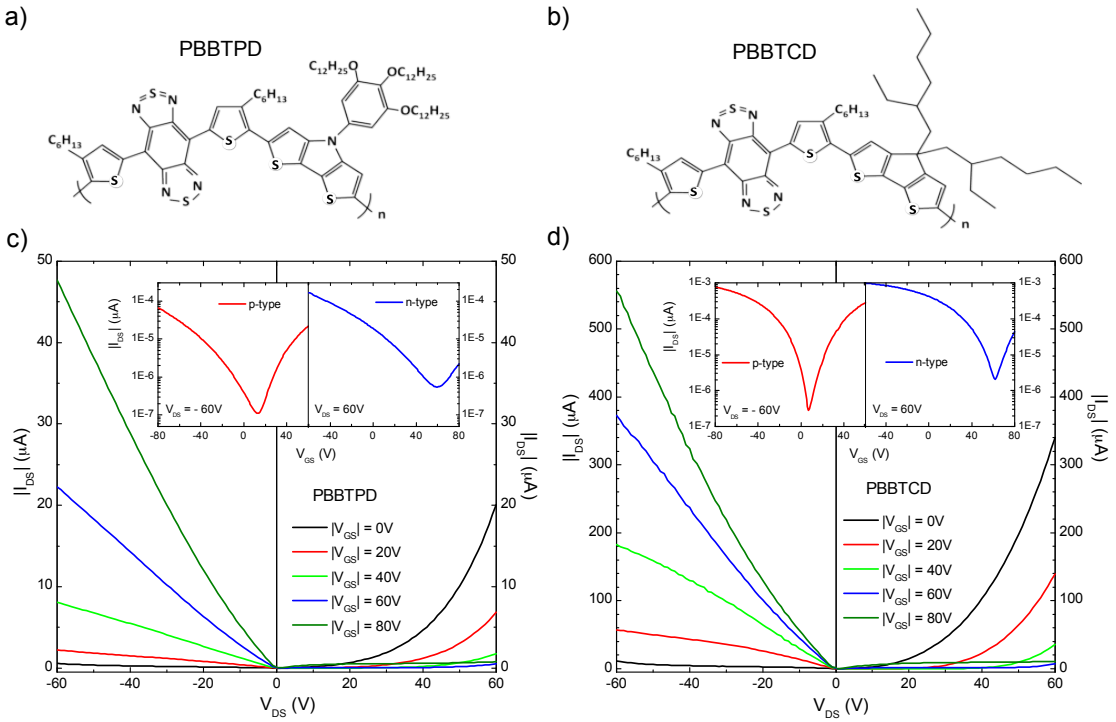

Figure 3.1: Top panels: chemical structure of a) PBBTPD and b) PBBTCD. Bottom panels: I-V output curves for a typical c) PBBTPD- and d) PBBTCD-based OFET with SiO_2 gate dielectric. Insets: OFET transfer characteristics using $|V_{DS}| = 60$V for p-type (red curve) and n-type (blue curve) operation.

observed transistor behavior is characteristic of ambipolar FET devices:[65,66] for small, negative gate voltage V_{GS}, holes are injected from the source electrode to form a relatively uniform charge distribution in the conduction channel. As the drain bias V_{DS} is increased beyond V_{GS}, the hole density at the drain decreases to zero, and the drain potential with respect to the gate surpasses the threshold for electron injection ($V_{GD} > 0$V neglecting trap states). Thus during ambipolar operation, there exist spatially separated regions of accumulated electrons and holes occupying a common conduction channel in the polymer. The contribution of both types of charge carriers to the source-drain current (I_{DS}) results in diode-like behavior seen in the I-V output characteristics. At high enough gate voltage such that both V_{GS} and V_{GD} are of the same polarity, the channel is populated with only one type of charge carrier, and transport becomes unipolar. For this configuration, conventional FET behavior is recovered with p-type (n-type) operation for $V_{GS} < 0$V ($V_{GS} > 0$V), demonstrating saturation of the drain current at high V_{DS}. The "V"-shape of the transfer curves (insets in Fig. 3.1c,d) is an additional hallmark of ambipolar charge injection, with the minimum signifying a transition from ambipolar to unipolar conduction.

Charge carrier mobilities were extracted using the conventional equation describing FET operation in the saturation regime:[24]

$$I_{DS} = \frac{1}{2}\frac{W}{L}\mu C_i(V_{GS} - V_T)^2 \tag{3.1}$$

with mobility determined from $\partial|I_{GS}|^{1/2}/\partial V_{GS}$. Unipolar transport regimes were used for this calculation, since during ambipolar operation it is difficult to distinguish the separate electron and hole contributions to the current. Average mobilities for electrons and holes, respectively, were μ_e=8.2x10^{-3} cm^{2}V^{-1}s^{-1}, μ_h=9.6x10^{-3} cm^{2}V^{-1}s^{-1} for PBBTPD, and μ_e = 0.11 cm^{2}V^{-1}s^{-1}, μ_h = 0.072 cm^{2}V^{-1}s^{-1} for PBBTCD, demonstrating ambipolar transport with similar p-type and n-type performance.[58] Due to the sensitivity of electronic transport to charge traps arising from film deposition and fabrication conditions, threshold voltages for electron injection tended to vary substantially among different devices.

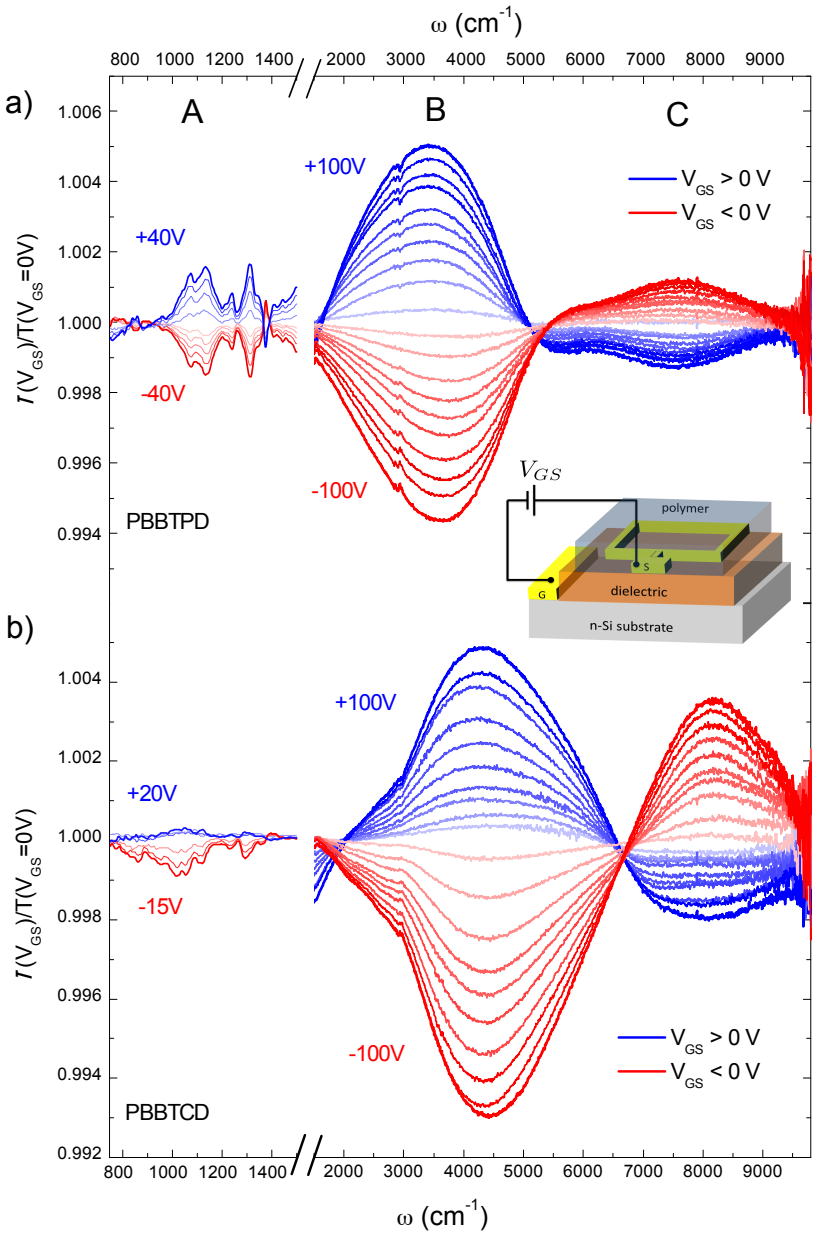

Figure 3.2: Voltage-induced change in transmission spectra $T(\omega, V_{GS})$ / $T(\omega, V_{GS}$=0V)) for structures employing a) PBBTPD and b) PBBTCD as the active semiconductor. Blue curves indicate n-type operation (V_{GS} >0V), i.e. electron injection; red curves indicate p-type operation (V_{GS} <0V), i.e. hole injection. Spectra from 750 - 1500 cm^{-1} are representative data for devices with Ta_2O_5 gate insulator, where strong absorption due to the substrate is absent. Inset in a) schematic of single-contact device architecture used for IR and capacitance measurements.

3.3.2 IR spectroscopy of BBT-based DA polymer OFETs

We used infrared spectroscopy to probe the electronic excitations associated with injecting both electrons and holes into DA polymer films. The use of a rectangular electrode structure enclosing the illuminated area (inset in Fig. 3.2) ensures an electrostatic charge configuration, equivalent to grounding the source and drain electrodes, while maximizing the IR signal. Figure 3.2a shows IR transmission spectra T(ω,V_{GS}) for a PBBTPD device plotted at various V_{GS}, normalized by T(ω,V_{GS}=0V). Typically, differential spectra ΔT(ω)/T(ω) are better suited than absolute T(ω) measurements for studying charge- and field-induced changes in IR transmission, which are usually extremely small (10^{-3} - 10^{-4}) and require very high accuracy. The red curves in Fig. 2 indicate p-type operation ($V_{GS} < 0V$), while the blue curves indicate n-type operation ($V_{GS} > 0V$). To facilitate the discussion, we denote three separate frequency regions in the spectra as regions A, B, and C, described in more detail below. Spectra are plotted in 10V increments except for region A in Fig. 3.2b (5V increments). Data in region A were obtained through transmission measurements for Ta_2O_5-based devices, while spectra in regions B and C were recorded for devices with SiO_2 gate insulator. SiO_2/Si provides an ideal oxide/substrate interface with extremely low leakage currents and long-term device stability. However, excitations in the polymer below 1500 cm^{-1} are obscured by Drude absorption in n-Si and phonon modes in SiO_2. For devices based on Ta_2O_5, a high-κ dielectric, in most cases no Drude absorption in the silicon is observed, and the oxide does not possess any IR-active phonons in the experimental range of interest.

We start with the features originating from hole injection (red curves in Fig. 3.2a) for negative gate voltage. In the range 750 - 1500 cm^{-1}, labeled as region A, several sharp absorption peaks (dips in transmission) are observed, a prominent absorption band centered at 3400 cm^{-1} defines region B, while a broad increase in transmission from 5000 - 9000 cm^{-1} is described as region C. The oscillator strength of all excitations systematically increases with the applied gate voltage.

The injection of electrons (blue curves in Fig. 3.2a) results in the appearance of features occurring at nearly the same frequencies compared to hole doping.

Interestingly, however, the change in oscillator strength for each excitation demonstrates the opposite dependence on the applied field: the absorptions in regions A and B are suppressed, whilst a new absorption appears in region C. Further increasing of the gate voltage to higher positive values leads to systematic suppression of the features in regions A and B, while strengthening the absorption in region C. All these effects mirror the evolution of the spectra with hole doping.

Figure 3.2b displays field-modulated transmission spectra for PBBTCD, a higher-mobility polymer of the same BBT-acceptor family. Similar IR features and field-dependence compared to PBBTPD are observed. Notable differences, however, include a slightly different lineshape and blueshift of the excitations in regions B and C. Additionally, the sharp resonances in region A occur at lower frequencies. Lastly, there is a more pronounced asymmetry in the strength of the modulation of the spectra, with positive gate-induced features being generally weaker than those for hole doping. The mirror-like behavior reflected in the IR spectra for both polymers is highly reproducible, and was observed in over 30 structures, consisting of both two- and three-terminal devices. The symmetry in the intensity of the positive and negative voltage-induced features is more common in PBBTPD devices, while the spectra tend to be more asymmetric in most PBBTCD structures. Later we discuss a possible connection of these differences to transport in the two polymers.

3.3.3 Ellipsometric characterization of polymer absorption edge

In order to explain the voltage dependence of the IR transmission spectra, it is important to understand the behavior of absolute absorption in the polymer films. We employed spectroscopic ellipsometry to obtain a detailed characterization of the absorption edge for both polymers, which occurs in the vicinity of the gate-induced features. Due to the limited device area, as well as other constraints imposed by field-effect devices (eg electrodes), ellipsometry was performed on thicker polymer films deposited on unpatterned silicon substrates. Figure 3.3 shows the absorption coefficient as a function of frequency, $\alpha(\omega)$, determined from

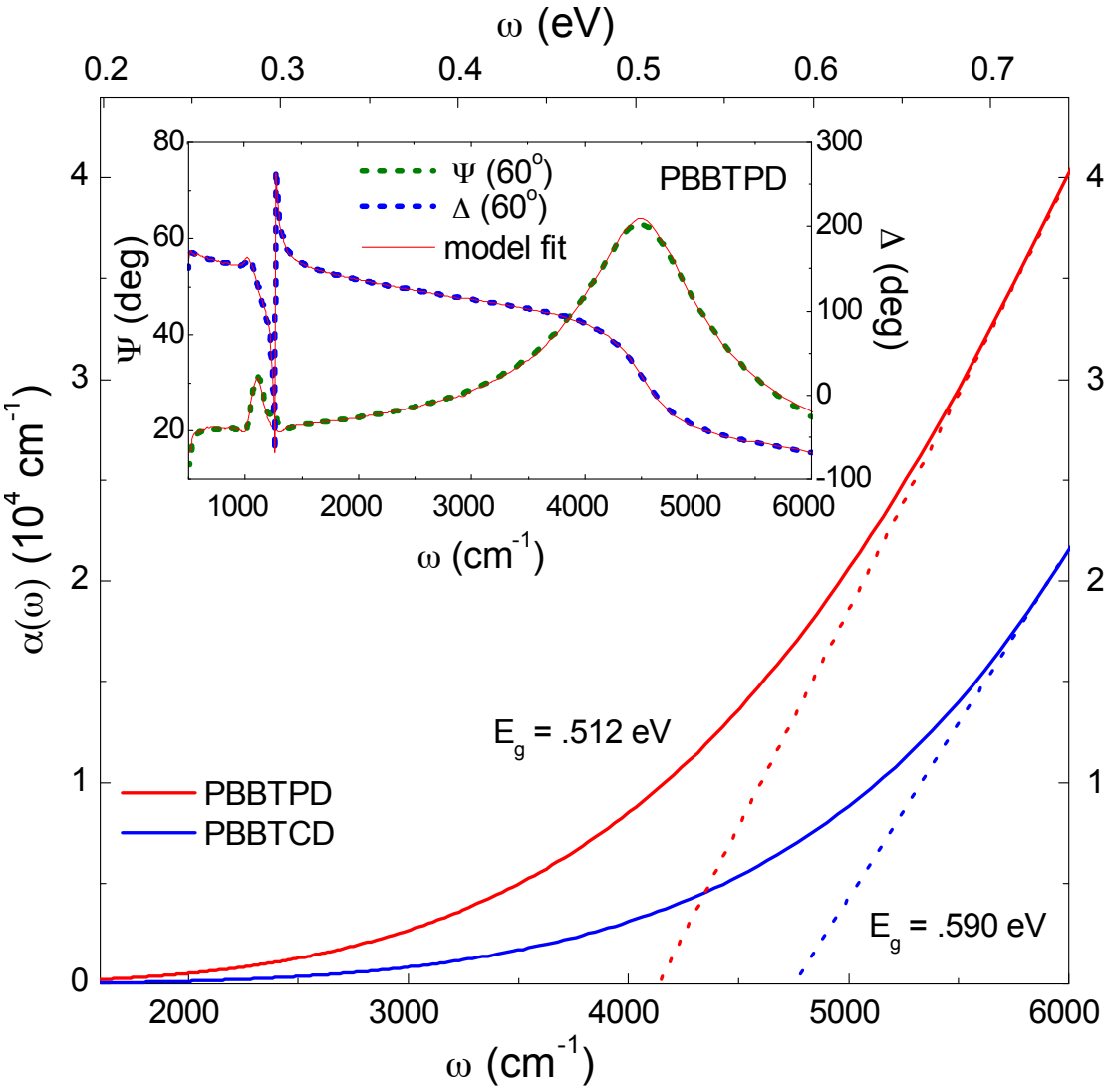

Figure 3.3: Absorption coefficient $\alpha(\omega)$ for PBBTPD (red solid line) and PBBTCD (blue solid line) thin films, obtained from modeling of ellipsometric data. Dotted lines indicate linear extrapolation of absorption edge to determine the energy bandgap E_g for each polymer. Inset: Experimental ellipsometry data Ψ (green dashed line) and Δ (blue dashed line) for PBBTPD on SiO_2/Si. Spectra were acquired at an incidence angle of 60° and are plotted with corresponding model fits (red solid lines).

analysis of the ellipsometric data as described in Section II. The complex refractive index $N = n + ik$ was extracted from a Cody-Lorentz oscillator model, whence $\alpha(\omega)$ was obtained via $k = \alpha c/\omega$. The optical bandgap E_g was extracted by extrapolating the linear portion of the absorption edge to the horizontal axis (red and blue dotted lines). The values of E_g obtained were 4,113 cm^{-1} (.51 eV) for PBBTPD and 4,758 cm^{-1} (.59 eV) for PBBTCD, which are very close to those observed in absorbance spectra.[58] Experimental and model ellipsometry data for PBBTPD on SiO_2/Si obtained at an incidence angle of 60° are shown in the inset of Fig. 3.3.

3.3.4 Raman spectroscopy

In addition to an ellipsometric analysis of the absorption edge, we carried out Raman spectroscopy measurements to assist in the examination of the sharp doping-induced peaks in region A of Fig. 3.2. The bottom panel of Figure 3.4 shows Raman spectra for thin films of PBBTPD (violet line) and PBBTCD (green line) on SiO_2/Si., while the top panel reproduces data from Fig. 3.2. Though spectra for both polymers show a similar pattern, Raman modes for PBBTCD are distinct from those of PBBTPD. Important to note is the large discrepancy in energies associated with the voltage-induced peaks in PBBTPD compared to PBBTCD, in contrast with the rather small variations in the Raman modes between the two polymers.

3.3.5 Quantifying carrier density from IR excitations and transient charging currents

In general, the optical functions of a material can yield important information about physical processes governing the dynamics of electrons and holes through the frequency sum rule $\int_0^\infty \frac{nc}{4\pi}\alpha(\omega)d\omega \propto \frac{N_e}{m_{eff}}$. This expression connects the density of charges N_e (with effective mass m_{eff}) contributing to the electromagnetic response, to the integral of the absorption coefficient over all frequencies.[67] In the spirit of this generic sum rule result, we define a quantity, ΔI, that relates

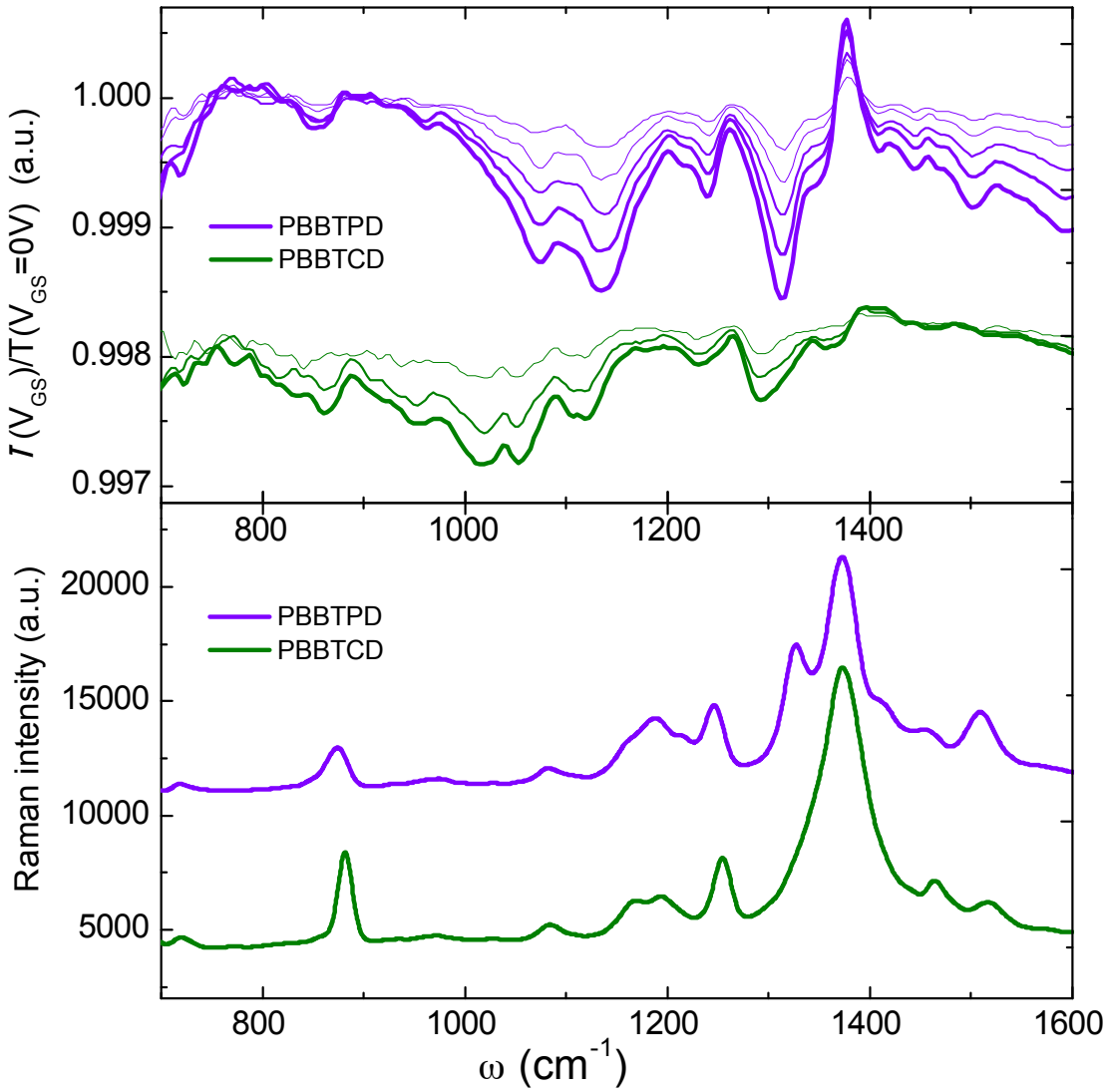

Figure 3.4: Top panel: Voltage-induced peaks for PBBTPD (violet curves) and PBBTCD (green curves) reproduced from Fig. 3.2. Bottom panel: Raman spectra for PBBTPD (violet line) and PBBTCD (green line) thin films on SiO_2/Si.

the injected charge carriers to the field-induced change in IR transmission as

$$\Delta I = \int_{1400}^{5200} \frac{T(\omega, V_{GS})}{T(\omega, V_{GS} = 0V)} d\omega, \tag{3.2}$$

where the limits of integration were chosen over the feature in region B near the onset of the absorption edge. Plotted on the left axis of Figure 3.5a is $|\Delta I|$ as a function of V_{GS} (red squares). ΔI very clearly evolves linearly with the applied electric field for both electron and hole injection.

For structures with SiO_2 gate insulator, it is safe to model device behavior as an ideal parallel plate capacitor, where the induced charge density increases linearly with the applied electric field.[16] We independently verified this assumption by acquiring transient current data $I_{GS}(t)$ for a PBBTPD-based device (Fig 3.5b), where $|V_{GS}|$ is applied as square wave pulses with a period of T=10s. The charging currents measured during the first few seconds of each pulse can be integrated to yield the total number of injected charges $Q = \int (I_{GS}(t) - I_L)dt$, and thus the 2D carrier density $n_{2D} = Q/A$, where I_L is the leakage current and the active device area is $A = 1\ cm^2$. n_{2D} as a function of V_{GS} is plotted on the right axis of Fig. 3.5a (black squares). Establishing the linear relationship between the applied electric field V_{GS} (i.e. injected charge carrier density) and the field-induced change in IR transmission ΔI is important for interpretations presented in the next section. The obtained values for n_{2D} are in good agreement with the maximum carrier densities typically achieved in OFETs employing oxide gate insulators.[16]

3.4 Discussion

The salient characteristic of pristine BBT-based copolymers is the exceptionally narrow energy bandgaps observed in absorbance measurements[58,59] and confirmed through our ellipsometric data plotted in Fig. 3.3. Gap values extracted from these data, 0.51 eV for PBBTPD and 0.59 eV for PBBTCD, are among the smallest for ambipolar DA conjugated polymers. Additionally, there is considerable broadening of the absorption edge, which is expected for a disordered, amorphous polymer thin film. The energy range associated with the disorder-induced band

tail states, and of the interband transitions in general, is relevant to the observed gate-induced transformations of the spectra.

3.4.1 IR-active vibrational modes

There are multiple processes that give rise to the features we observe in the IR transmission data in Fig. 3.2. We start this analysis with a discussion of the resonances in region A. The addition of charge carriers to a neutral polymer commonly leads to the formation of infrared-active vibrational modes (IRAVs): distortions in the polymer backbone due to injected charges.[34] The excess charge couples to symmetric Raman modes, inducing a transition dipole moment that renders these modes IR-active. The manner in which sharp peaks induced by hole injection in region A of Fig. 3.2 intensify systematically with increasing gate voltage is consistent with previous spectroscopic studies of conjugated polymer OFETs.[16] Observation of a distinct IRAV spectrum each for PBBTPD and PBBTCD is a natural consequence of the different chemical structure, also reflected in the Raman data shown in Fig. 3.4. The lower frequencies associated with IRAVs in PBBTCD, indicative of weaker localization of charge carriers, is discussed later.

The systematic increase in transmission of IRAV features for positive gate voltages remains curious. The amplitude mode (AM) formalism[34,68] and subsequent theoretical efforts,[69,70,71,72] aimed at providing a model for IRAV bands in polymers, do not discriminate between the electrons and holes. However, studies investigating electrochemical n- and p-doping of the same polythiophene hosts reveal distinct IRAV modes induced for positive and negative charge carriers.[73] Thus, one would expect to observe a different series of absorption peaks for electron injection, as opposed to suppression of the same absorption features. The observed behavior is consistent with the assumption that IRAV absorption persists in the ungated polymer as will be detailed below.

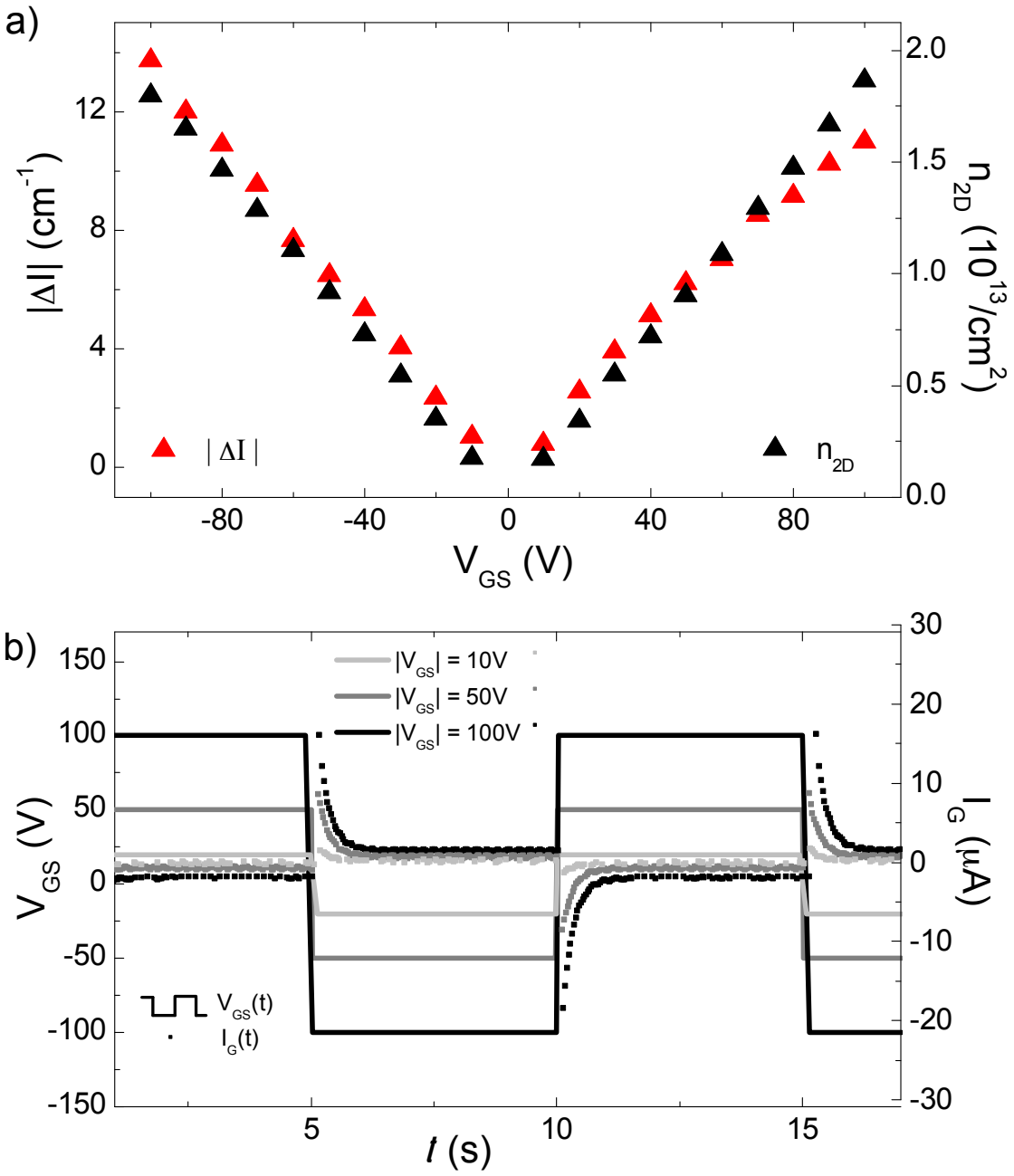

Figure 3.5: a) Left axis: Field-induced change in transmission, $|\Delta T|$ (red triangles), integrated from 1400-5200 cm^{-1} and plotted as a function of V_{GS}. Right axis: 2D density of induced electrons or holes, n_{2D} (black triangles), as a function of V_{GS}. n_{2D} was obtained by integrating the transient current I_G in b), after subtracting leakage, and assuming an accumulation layer thickness of d = 2nm and an active area of A = .5 cm^2. b) $I_G(t)$ data for a PBBTPD thin-film device, applying $|V_{GS}| = 10$ (light grey), 50 (dark grey), and 100V (black) as a pulse waveform with period T=10s.

3.4.2 Interpretation of polaronic IR features

The assignment of the broad mid- and near-IR features (regions B and C) is less straightforward. Typically, concomitant with IRAVs are large absorption bands signifying optical transitions to mid-gap localized states, observed in many previous spectroscopic studies of conducting polymers.[37,1,33,36,31,32,35] Formation of these localized states is related to geometrical relaxation (lattice distortion) in non-degenerate ground state polymers due to excess charges, usually described as polarons or bipolarons. In addition to unique IRAVs, a distinct polaron feature is expected to arise each from electron and hole injection, confirmed through chemical doping studies in Ref. (73). Recent data on polyselenophene-based ambipolar OFETs from Chen et al. also reveal spectroscopic evidence of electron and hole polaron absorption, in response to an applied gate bias.[74] The intensity of these excitations increases at the expense of the (bleached) neutral absorption. In other intrinsically ambipolar systems, such as monolayer and bilayer graphene, either polarity of gate voltage results in increased absorption at far- and mid-IR frequencies.[75,76,77,78,79] This expected behavior of both electron and hole-induced absorption stands in contrast with what we observe in our data. The mirror-symmetric form of the spectra in Fig. 3.2 is more in line with what has been seen recently in heavily-doped semiconductors.[80]

It is possible that these IRAV and broad excitations persist even in the ungated film due to an intrinsic charge-transfer mechanism during polymerization, or alternatively due to unintentional doping from extrinsic factors such as oxidation or trapping.[81] If there is an already-present hole-induced polaron band, the act of injecting electrons by gating reduces the number of positively-charged polymer segments, thereby suppressing the intensity of this broad absorption feature. The pronounced symmetry of the IR data for gated structures, with respect to the polarity of V_{GS}, would thus be the result of increasing or decreasing the oscillator strength of extrinsic hole-induced absorptions. In a similar vein, the behavior of the spectra in region C could reflect bleaching/restoration of the neutral absorption as holes or electrons are injected, respectively. In essence, the primary consequence of injection of electrons in the mid-IR spectra is to compensate for holes that

are already present in our polymers. Based on the symmetry reflected in the data, the charge neutrality point is never reached within the range of V_{GS} we apply. Additionally, an initial population of excess holes implies the existence of IRAVs without an applied field. However, IRAV modes could not be definitively distinguished from intrinsic IR vibrational absorptions in absolute transmission measurements of the polymer film.

The presence of mobile holes in the ungated film has implications for the prospect of ambipolar device operation. Electron transport is especially sensitive to the presence of trap states, and such charged defects would assuredly compromise device performance by capturing mobile electrons. The consistency of the symmetric behavior in the IR transmission data presents an interesting conundrum to the origin of the intrinsic ambipolarity in BBT-based copolymers. Though electron transport varied greatly across structures with source and drain electrodes (for which OFET I-V characteristics could be measured), both ambipolar transport and symmetric IR spectra have been observed for at least a few devices. This would seem to rule out the possibility of degradation before every spectroscopic measurement, due to ambient air exposure. The simplest physical picture of enhancement/suppression of hole-polaron and IRAV absorption, seemingly evident from the IR spectra, implies that movement of the Fermi level in response to charge injection takes place entirely within a polaron band in the vicinity of the HOMO band edge. The possibility of such a system sustaining electron transport with mobility comparable to holes is dubious at best, calling for perhaps more complicated interpretations of the electronic structure of these particular DA materials.

3.4.3 Inhomogeneous phase-separated conducting polymer

In light of the observation of IR features associated with localized states, as well as transport data demonstrating relatively high carrier mobility, we posit the prospect of phase separation and coexistence in the copolymer. Many theoretical models of conducting polymers involve a continuous electronic transition from localized to itinerant charge carrier motion with doping, as trap states are eventually filled up to the "mobility edge."[82,33,83] An underlying assumption is

that of a homogeneous film, a questionable postulate. Perhaps a more realistic picture of electronic transport in disordered polymer films is the one allowing for coexisting regions dominated by either localized or delocalized ("metallic") transport. Indeed phase coexistence of both localized and delocalized states has been observed in highly-doped polyacetylene,[33] polyaniline,[83,45] and P3HT.[23,84] Our spectroscopic probe interrogates the higher energy bound states characteristic of localized charges, while OFET transport data are dominated by mobile carriers.

The response of delocalized carriers to light excitation typically manifests in increased far-IR Drude-like absorption.[27,67,33,45,83,23,84] In polyaniline, a significant metallic optical response was observed concurrent with IRAV modes, and was modeled as a conductor with molecular scale disorder and mesoscale inhomogeneity associated with phase separation.[45] Such a Drude-like response in the DA polymers investigated here would likely be masked by the overwhelmingly strong free-carrier absorption in the n-doped silicon substrate. Also consistent with the notion of coexisting localized and itinerant carriers is the weaker suppression of absorptions in PBBTCD devices for electron injection. IRAVs in PBBTCD have smaller energies and are generally less intense compared to PBBTPD, reflecting a smaller degree of localization, consistent with transport measurements that show an order of magnitude higher electron and hole mobility. Detailed studies of doping-induced vibrational modes in conducting polymers show that the degree to which IRAV frequencies are red-shifted from the symmetric Raman modes is related to a "pinning parameter" that characterizes the localization of the injected charge carriers.[85,86,70] Theoretically, a lower vibrational frequency (i.e. smaller force constant) reflects smaller electron-phonon coupling, leading to improved charge transport. Additionally, if suppression of the polaron absorption in region B is associated with trapped electrons, the symmetry in the IR data is an indicator of compensation by holes. Thus, the 'weaker' suppression of hole-induced absorptions for positive gate voltages in PBBTCD suggests an increase in the population of mobile carriers, leading to better electron transport.

3.4.4 Electroabsorption (Stark Effect)

Lastly, we comment on the possible role of field-induced modification of the band edge states (electroabsorption), i.e. the Stark effect. The observed effects in regions B and C of Fig. 3.2 clearly occur in the vicinity of the broadened band edge. The apparent blueshift of this structure for PBBTCD, which possesses a slightly larger bandgap than PBBTPD, further strengthens the connection between these features and the polymer absorption edge. Electroabsorption (EA) spectra of conjugated polymers are usually interpreted in terms of either the linear or quadratic Stark effect.[87,88,89,90,91,92,93,94,95,96,62] The latter originates from induced dipoles, as the applied electric field mixes the low energy states of odd parity with the excited state continuum at higher energies.[90] The energy shift associated with a quadratic stark shift is independent on the sign of the applied field, which is inconsistent with the linear behavior we observe in Fig. 3.5a. The linear Stark effect, which is due to permanent dipoles, can explain the symmetric form of the broad absorptions, provided there is a large intrinsic built-in electrical dipole moment, as well as interfacial ordering at the semiconductor/insulator interface.[97] The origin of such a dipole, as well as a mechanism by which ordering near the interface could occur, is unclear. We carried out density-functional theory (DFT) calculations for isolated donor-acceptor molecules using the Octopus code[98] with PBE[99,100] functionals, and we do find a significant ground state dipole moment for both PBBTPD (3.47 Debye) and PBBTCD (1.31 Debye), as well as a strengthening of the dipole in the dimers.[101] However, compared to the more plausible picture of polaron absorption, and the failure of the linear Stark effect to explain the behavior of IRAVs, we feel that any electroabsorptive effects are most likely minor and/or unnoticeable.

3.5 Summary

We have systematically investigated the infrared response of charge injection in ambipolar OFETs based on narrow-gap DA polymers PBBTPD and PBBTCD. In both polymers, hole doping produces several sharp absorption peaks

in the range 800 - 1400 cm^{-1} associated with injected charges and identified as IRAVs. Additionally, hole injection results in the appearance of a broad absorption near the band edge in both PBBTPD and PBBTCD, followed by an increase in transmission above the energy gap. For positive gate voltages, the intensity of charged excitations occurring at the same frequencies weakens with increasing field, leading to a mirror-like behavior in the IR spectra (i.e. hole-induced absorptions are suppressed). An observed blueshift of field-induced IR features in PBBTCD is consistent with the slightly larger energy bandgap, and suggests the origin of the broad structures to be closely linked to the absorption edge of the HOMO-LUMO transition.

The symmetry of the IR transmission data with respect to the polarity of the gate voltage presents a challenge to understanding the electronic excitations associated with ambipolar charge injection in narrow-gap polymers. The totality of our data indicates a significant self-doping of holes that is modified by charge injection. Clear observations of both hole and electron transport with high carrier mobility strongly suggest an inhomogeneous, phase-separated conducting polymer. A high-resolution real space probe is necessary to resolve such inhomogeneities, and explore the molecular effects of electron and hole injection on the electronic structure of BBT-based DA copolymers.

3.6 Acknowledgements

The research at UCSD was supported by AFOSR Grant No. FA9550- 09-1-0566 and University of California. The sample preparation for FET and IR studies was carried out at UCSB with support from DARPA through a HARDI program). Chapter 3, in full, is a reprint of material as it appears in O. Khatib, J. D. Yuen, J. Wilson, R. Kumar, M. Di Ventra, A. J. Heeger, D. N. Basov, 'Infrared spectroscopy of narrow gap donor-acceptor polymer-based ambipolar transistors,' Physical Review B 86, 195109 (2012). The dissertation author was the primary investigator and author of this publication.

Chapter 4

Infrared microscopy and imaging of high mobility narrow-gap DA copolymers

A resurgence in the use of the donor-acceptor (DA) approach to synthesizing conjugated polymers has resulted in a family of high-mobility ambipolar systems with exceptionally narrow energy bandgaps below 1 eV. The ability to transport both electrons and holes is critical for device applications such as organic light-emitting diodes (OLEDs) and transistors (OLETs). Infrared spectroscopy offers direct access to the low-energy excitations associated with injected charge carriers. Here we use a diffraction-limited IR microscope to probe the spectroscopic signatures of electron and hole injection in the conduction channel of an organic field-effect transistor (OFET) based on ambipolar DA polymer polydiketopyrrolopyrrole-benzobisthiadiazole (PDPPBBT). We observe distinct polaronic absorptions for both electrons and holes, and spatially map the carrier distribution from the source to drain electrodes for both unipolar and ambipolar biasing regimes. For ambipolar device configurations, we observe the spatial evolution of hole-induced to electron-induced polaron absorptions throughout the transport path. Our work provides a platform for combined transport and infrared studies of organic semiconductors on micron length scales relevant to functional devices.

4.1 Introduction

Organic semiconductors continue to evolve as a viable and attractive alternative to conventional silicon-based electronics.[24] Much effort is devoted to reducing and tuning energy bandgaps between the highest occupied molecular orbital (HOMO) and lowest unoccupied molecular orbital (LUMO) levels in π-conjugated polymers to improve performance.[54,55,56] Specifically, the donor-acceptor (DA) approach to synthesizing polymers has led to a new generation of high-mobility ambipolar systems, a necessary precondition for many transistor, photovoltaic, and light-emitting device applications.[51,52,53,57] Recently, DA polymers based on acceptor benzobisthiadiazole (BBT)[53,58,59] and donor diketopyrrolopyrrole (DPP)[102,59,103,104,105,106] have demonstrated strong ambipolarity as well as exceptionally narrow energy badgaps as small as 0.5 eV.[102] The highest field-effect mobilities in these systems have surpassed 1 $cm^2V^{-1}s^{-1}$ for both electrons and holes.[102,51] Despite much recent progress, however, there remains an incomplete understanding of the fundamental nature of charge transport and dynamics, especially in DA systems that accomodate both types of carriers.

Infrared and optical spectroscopy is a valuable tool for probing the fundamental charged excitations in conducting polymers.[41,21] Spectroscopic probes have direct access to microscopic details of the electronic states without interference from extrinsic effects that often complicate electrical measurements of field-effect devices, such as contact resistance.[24,19] The electronic structure of these quasi-1D systems is significantly modified by the presence of additional charges, giving rise to localized states in the forbidden energy gap. The optical transitions to these sub-bandgap states characterize the nature of the mobile charge carriers in organic semiconductors. Polaronic absorption in polymers is very well established.[36,21,41,107,85,16,18] However, very few studies thus far have explored spectroscopically both electron and hole polarons in the same system, made possible by the emergence of ambipolar DA polymers. In recent work on homopolymer polyseleneophene,[74] using charge-modulation spectroscopy (CMS) Chen et al. studied the origin of the different transport characteristics of electrons and holes in a semicrystalline ambipolar polymer. Similar charge-induced absorptions, in the near-IR

just below the bandgap, were observed for both types of carriers.[74] Such extensive studies for ambipolar copolymer systems, where the choice of donor and acceptor molecules can lead to widely varying electron/hole properties, are still lacking.

Previously, we investigated the infrared response of a new generation of small bandgap DA copolymers[108] based on BBT. In this work, we expand on these studies in a high-mobility narrow gap DA system polydiketopyrrolopyrrole - benzobisthiadiazole (PDPPBBT). Using infrared spectroscopy, we observe distinct electronic absorptions for electron and hole polarons accumulated in electrostatically-doped PDPPBBT. Further, using a diffraction-limited IR microscope, we register the evolution of the dynamic IR response along the conduction channel during device operation. In conjunction with IR measurements, we measure OFET transport in-situ. We are thus able to directly link macroscopic transistor behavior to the micro-spectroscopic signatures of electrons and holes in the polymer. Based on the peak position and strength of the IR absorptions, we are able to image the charge density throughout the transistor channel. We create a spatial map of the carrier distribution for several biasing configurations spanning unipolar electron and hole operation, as well as ambipolar device regimes, where both electrons and holes coexist in the transport path. Coexistence of electrons and holes in a single polymer layer forms the basis for emission in devices such as organic light-emitting diodes (OLEDs) and transistors (OLETs). Our experimental approach sets the stage for combined transport/optics studies of the low-energy physics of polymers and molecular crystals on micron length scales important to practical devices.

4.2 Experimental details

PDPPBBT (Figure 5.2a) was synthesized via Suzuki coupling between the donor (DPP) and acceptor (BBT) moieties following a well established procedure.[58,102] Thin polymer films were spin coated onto IR-transparent 20-30 Ω-cm n-doped Si wafers, serving as the back gate, with a 300 nm SiO_2 (ϵ= 3.9) gate insulator. Electrodes were patterned using standard photolithography and were formed with e-beam evaporation of 3 nm of nickel followed by 47 nm of gold.

Substrate surfaces were passivated with decyltrichlorosilane (DTS) before polymer deposition to lower the density of interfacial trap states.

Source and drain contacts were patterned in an interdigitated device structure with a channel width of 17 mm and length of 200 μm, allowing for spectroscopic monitoring of the gate-induced changes in the IR transmission/reflection on diffraction-limited length scales (detailed below). Transistor measurements and electrical characterization of devices were obtained with dual Keithley 2400 Sourcemeters.

Figure 5.2b shows a schematic of the experimental setup. Infrared spectra were acquired using a diffraction-limited IR microscope (Bruker LUMOS). Broadband light from a SiC globar source is focused onto the sample surface using an 8x Schwartzchild objective. In reflection mode, the return path of the reflected IR beam is along the other half of the objective, while transmission mode uses a bottom illumination configuration (Fig. 5.2b). The transmitted/reflected IR light is then focused onto a small-area (d=100μm), mid-band (650-6500 cm^{-1}) HgCdTe (MCT) detector. In all measurements, we observe similar behavior in IR transmission and reflectance, however in this work we only report transmission data.

The minimum beam size is determined by an optically transparent, IR opaque software-controlled motorized knife-edge aperture. For electrostatic IR measurements (V_{DS}=0V), data were recorded with a spectral resolution of 8 cm^{-1} and a beam width spanning the distance between the source and drain electrodes (200μm). For microscopy, the beam size and spectral resolution were reduced to 20μm and 16 cm^{-1}, respectively. The motorized stage was translated in increments of 20μm between the source and drain, to map out the microscopic IR response during device operation.

To observe gate-induced effects in OFETs, we adapted an Oxford microcryostat (MicrostatHe2) to fit the microscope stage, allowing us to perform repeated IR and transport measurements in high vacuum and low temperature if desired. This was necessary to minimize carrier trapping in the devices, especially for electron transport as we detail below, and achieve a high signal-to-noise ratio.

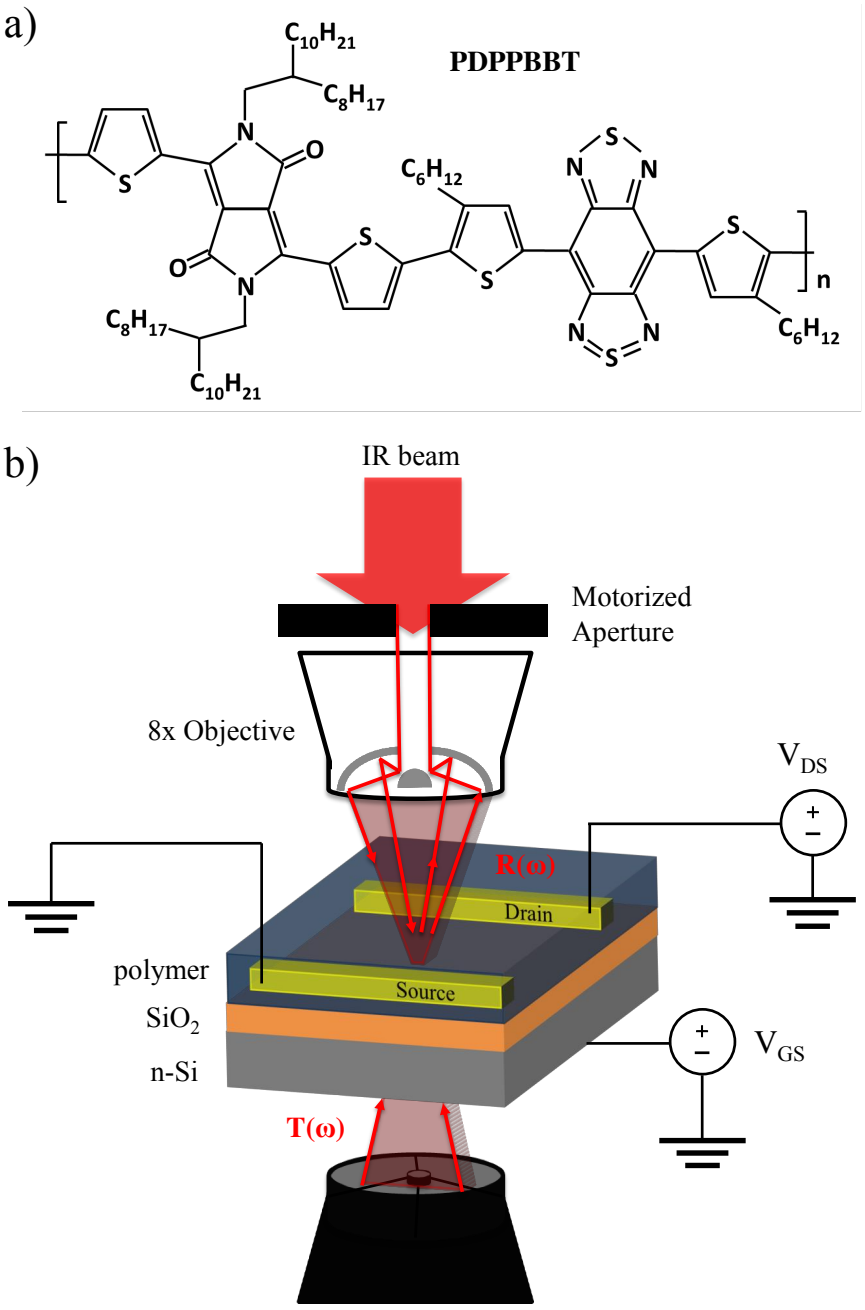

Figure 4.1: a) Chemical structure of PDPPBBT. b) Experimental setup allowing for electrical transport measurements and IR micro-spectroscopy along the conduction channel between the source and drain electrodes. Small arrows denote the optical path of the IR beam in both reflection (top-illumination) and transmission (bottom-illumination) modes.

All data reported here were obtained at a pressure of 10^{-6} mbar and at room temperature. The cryostat was fitted with 1.5mm IR-transparent KBr windows and Manganin wires for electrical connections. The entire microscope was encapsulated in a nitrogen purge box.

We note here that introduction of thick windows into the optical path of the microscope shifts the focus of the IR beam. Since the index of refraction of KBr is flat from the mid-IR through the visible energy range, we do not expect a discrepancy between the IR and visible focus. For transmission measurements (bottom illumination) we adjusted the microscope condensor to account for both the KBr window and thick Si substrate. Our ability to resolve spectral shifts on 20μm length scales affirms the validity of our adjustments.

4.3 Results and discussion

4.3.1 Transport

Figure 4.2 shows the in-situ output characteristics of the PDPPBBT OFET prepared for IR microscopy. We observe typical ambipolar transport behavior:[65,66] diode-like evolution of the drain current at low to moderate gate voltages, and strong electron or hole saturation currents at higher gate bias. Charge carrier mobilities were calculated in the saturation regime during unipolar operation via the standard equation:[24] $I_{DS} = \frac{1}{2}\frac{W}{L}\mu C_i(V_{GS} - V_T)^2$, with mobility determined from $\partial|I_{GS}|^{1/2}/\partial V_{GS}$.

For the device characteristics shown in Fig. 4.2, the extracted room temperature electron and hole mobilities were μ_e=0.04 $\mathrm{cm^2V^{-1}s^{-1}}$ and μ_h=0.02 $\mathrm{cm^2V^{-1}s^{-1}}$, respectively. Electron transport comparable to or stronger than holes is often seen in the DPP family of copolymers,[102] consistent with our extracted values. However, these values are quite low compared to typical DPP-based OFETs, which often have electron and hole mobilities surpassing 1 $\mathrm{cm^2V^{-1}s^{-1}}$.[51,103,104,105,106] We attribute the low field-effect mobility of the device studied here to a very high density of charge traps at the oxide interface, typically the result of exposure to ambient air and water moisture. The finite time required

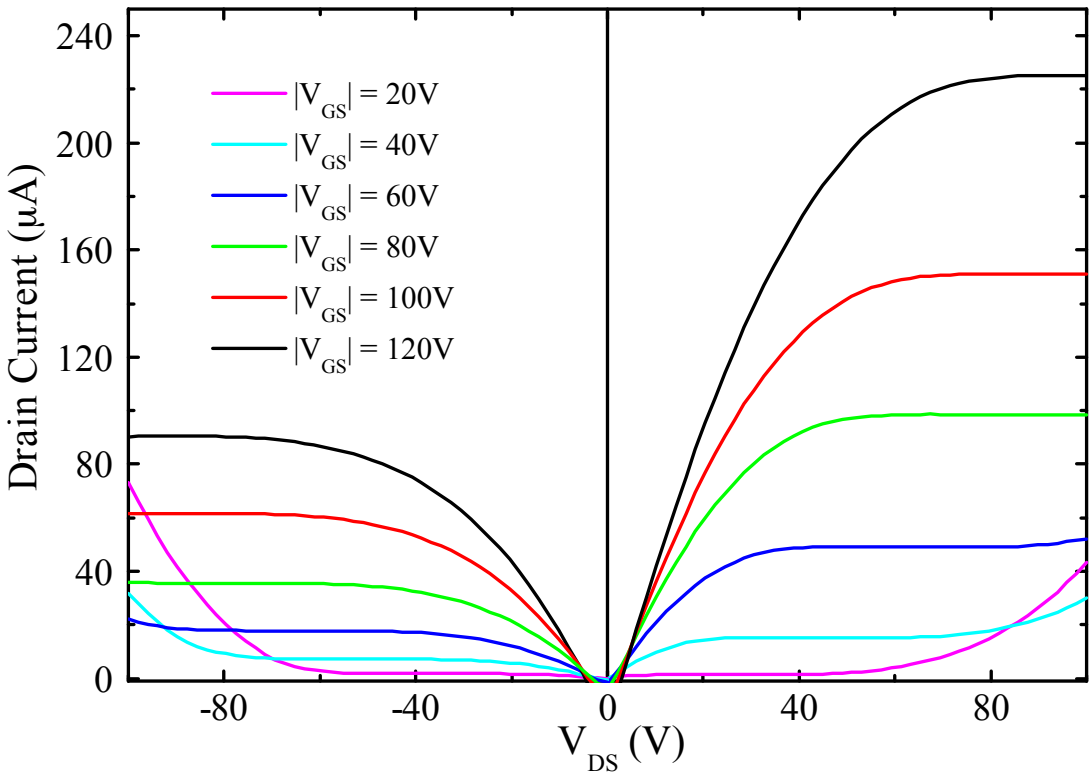

Figure 4.2: In situ I-V characteristics for SiO_2-based PDPPBBT device mounted in IR microscope. Electron and hole mobilities of $\mu_e = 0.04$ $cm^2V^{-1}s^{-1}$ and $\mu_h = 0.02$ $cm^2V^{-1}s^{-1}$, respectively, were extracted from the saturation regime during unipolar FET operation.

to mount and wire the sample in the micro-cryostat (roughly 30 minutes) in a quasi-purged environment ensures a small amount of inevitable exposure to ambient air, leading to a higher trap density.

We found severe carrier trapping for both electron and hole injection, indicative of bias stress: the trapping of injected charges, understood to be diffusion into the oxide layer.[109] Bias stress results in many trapped charges at the polymer/oxide interface, screening of the applied electric field, and a subsequent shift in the threshold voltage as a function of time.[74] The manifestation of trapping in the IR measurements, where repeated voltage applications are necessary, is discussed later. We were able to mitigate spurious effects of charge trapping by reversing the applied bias between measurements. This was confirmed by remeasuring I-V characteristics and monitoring the leakage current. We emphasize the importance of maintaining a very low pressure environment (10^{-6} mbar in our experiments) by use of a cryostat to minimize the role of trapping.

4.3.2 IR spectroscopy of PDPPBBT (electrostatic charge injection)

Figure 4.3 shows the field-induced changes in IR transmission for a PDPPBBT OFET. Data are plotted as negative differential spectra (i.e. absorption):

$$-\frac{\Delta T}{T}(\nu) = 1 - \frac{T(V_{GS})}{T(V_{GS} = 0V)} \tag{4.1}$$

where T(ν) is the absolute IR transmission. The color scheme adopted previously[108] and used throughout this manuscript labels positively charged (hole) excitations with red curves, and negatively charged (electron) excitations with blue curves. In this electrostatic configuration, the source-drain bias is zero, resulting in a large uniform spatial distribution of holes (electrons) in the channel for V_{GS} $<$ ($>$) 0V.

At high gate voltages, we find strongly resonant IR absorptions associated

with both injected electrons (V_{GS} = +120V) and holes (V_{GS} = -120V). At low energies, an absorption tail extends to just below 2000 cm^{-1}, with several sharp peaks superimposed. In the range 2000 - 5500 cm^{-1}, we observe very broad absorption bands, while at higher energies the absorption drops below zero (indicating a significant increase in IR transmission).

The low energy gate-induced increase in absorption is understood to be dominated by the free carrier response in the Si substrate, while the large feature at 1100 cm^{-1} is attributed to the SiO_2 oxide layer.[16,18] The smaller peaks superimposed on the substrate absorption, however, are infrared-active vibrational modes (IRAVs). These are symmetric raman modes in the polymer made IR-active by coupling to injected charges.[34,68,16,73] IRAVs are most evident in the absorption spectra for the hole-doped polymer (red curve in Fig. 4.3) where the substrate interference in minimal, but are otherwise too difficult to discriminate from the background and only briefly discussed.

The broad absorption bands above 2000 cm^{-1} are attributable to polarons: a result of adding free carriers to a neutral polymer chain. Polarons are formed when injected charge carriers distort the local bond arrangement of the polymer backbone, creating an energy well and resulting in self-localization. These energy minima create bound states in the bandgap, leading to the characteristic sub-gap absorption features. The bottom inset in Fig. 4.3 shows a schematic of the optical transitions for a single (a) positive or (b) negative charge added to a polymer chain, as well as the neutral HOMO-LUMO transition. The difference in energy between the polaronic states and the HOMO and LUMO orbitals indicates the energy gained by the system from the geometrical relaxation associated with the lattice distortion.[36,31,32]

IRAV and polaron spectral features are a hallmark of conducting polymers, and are very well understood in the context of both electrochemical and electrostatic doping.[53,59,37,1,33,36,31,32,35] The decrease of the gate-induced change in absorption below zero at energies just above the polaronic response is indicative of polymer bleaching. Indeed, the population of charged molecules increases with doping at the expense of the neutral $\pi - \pi^*$ absorption (bottom inset in Fig. 4.3)

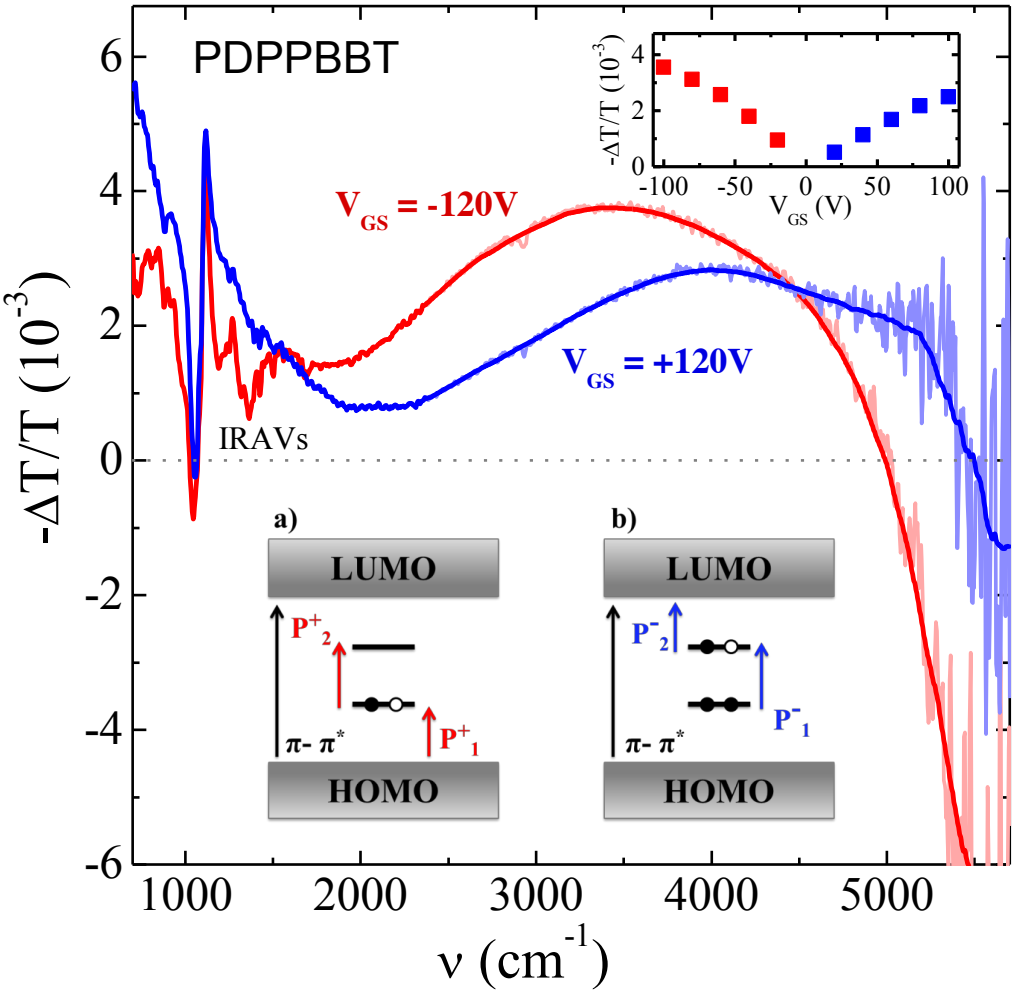

Figure 4.3: Differential transmission spectra ΔT/T for DPPBBT OFET. Red (blue) curves denote the field-induced absorption from a uniform accumulation of a high density of hole (electron) polarons in the conduction channel. The sharp peaks in the 900-1600 cm^{-1} range are infrared-active vibrational modes (IRAVs). The solid lines at higher energies represent averaged curves overlaying raw experimental data. Top inset: strength of peak absorption (ω_h = 3413 cm^{-1}, ω_e = 3981 cm^{-1}) as a function of gate voltage V$_{GS}$. Bottom inset: schematic of allowed optical transitions for a single a) hole and b) electron polaron state, as well as the neutral $\pi - \pi^*$ absorption between the HOMO and LUMO. Based on the peak energies in the experimental data, we ascribe the associated hole and electron absorption bands to the P_2^+ and P_1^- transitions, respectively.

that defines the energy gap. Thus, from the IR spectra we obtain a small bandgap of .62 eV (5001 cm^{-1}) for this PDPPBBT film, and ascribe the field-induced absorptions to the P_2^+ and P_1^- transitions for hole and electron polarons, respectively. The weaker bleaching of the neutral absorption under positive gate voltage is likely because some of the increase in transmission is offset by the high energy tail of the electron polaron absorption occuring concurrently. The strength of the absorption decreases linearly with applied gate bias, shown in the top inset of Fig. 4.3.

We find a significant difference in absorption energies between electrons and holes in the IR spectra in Fig. 4.3. The electron polaron absorption (blue curve) has a peak energy of 3981 cm^{-1}, while the hole polaron (red curve) peak occurs at 3413 cm^{-1}. The difference in polaronic peak energies is interesting in that it reflects an intrinsic asymmetry in the electron and hole wavefunctions in the polymer structure. In DA polymers, the degree of ambipolarity is intimately tied to the constituent donor and acceptor moeities. As different molecules are substituted into the copolymer structure, the HOMO and LUMO energy levels can shift significantly, affecting the bandgap, environmental stability, and band offsets determining the charge injection properties for various metal contacts.[51,52,53,54,55,56,102] Electronic transport, especially, is extremely sensitive to the choice of donor. The emergence of high-mobility DA polymers with strong electron and hole transport is a result of both HOMO and LUMO electron orbitals that are often well delocalized over the entire DA molecules.[53,52]

We can infer from the difference in peak energies that the electron polaron states are more weakly bound, and lie slightly closer in energy to the extended states than the hole polarons. This is also reflected in the higher electronic mobility we observe in transistor characteristics in Fig. 4.2, and much higher drain current for a given gate voltage, compared to holes. Our observations are consistent in general with the strong electron transport commonly observed in DPP-based copolymers. Slight shifts occur in the absorption peak energies for lower gate voltages, but these are much smaller than the energy difference between electron and hole polarons. Additionally, though plagued by a large background, the n-induced IRAVs appear to be much weaker than those for holes, also indicating a smaller

degree of localization. Thus, with our spectroscopic probe we are afforded direct access to microscopic details of the electronic structure, and fundamental differences in electron and hole behavior that are not available from transport measurements alone due to extrinsic effects (contact resistance, trapping, etc).

To conclude this section, we comment on our previous studies investigating a similar class of small bandgap polymers based on BBT,[108] discussed in Chapter 3. We found a remarkable symmetry in the IR spectra for both positive and negative gate voltages that we originally attributed to the existence of a self-doped polymer. We did not find significant absorption for positive gate voltages attributable to mobile electrons, and thus concluded a hole-dominated polymer despite often showing balanced ambipolar OFET transport. We now understand the origin of this self-doping to be due to severe electron trapping, resulting in a highly hole-doped 'off' state ($V_{GS} = 0V$) to maintain electrostatic balance. The symmetry seen in the IR data is a result of enhancement/suppression of an existing hole polaron absorption in the unbiased polymer.

The work presented in this Chapter, where we observe distinct spectral features for both conducting electrons and holes, underscores the need for an extremely low pressure environment ($< 10^{-5}$ mbar) afforded to us by using a high vacuum cryostat. We were unable to reproduce data shown in Fig. 4.3 in our broadband FT-IR spectrometer, where the ambient pressure is 2 mbar. Such a drastic dependence on ambient conditions indicates that charge trapping from water moisture and ambient air dominates the bias stress in these small-gap DA polymer devices, as well as trap states from the SiO_2 interface.[109,110,74,111,82,112]

4.3.3 Diffraction-limited IR microscopy of PDPPBBT OFET

Having established the spectral features associated with mobile electrons and holes in PDPPBBT, we employed IR microscopy to probe the charge injection landscape and dynamic response with 20 μm spatial resolution, much smaller than the OFET source-drain separation (d=200μm). For various voltage configurations, we expect very different carrier distributions in the transistor channel, especially

during ambipolar operation when both negative and positive charges contribute to the current.

Figure 4.4a shows representative IR absorption microscopy spectra for the PDPPBBT device biased in the ambipolar regime, where V_{GS} = +80V and V_{DS} = +120V, as a function of position. The format of Fig. 4.4a is a 3D plot using a logarithmic color scale to indicate the strength of absorption, and a 2D colormap projection of the IR spectra in the base plane as a visual aid. Starting from the source (x = 0μm), we find strong electron polaron absorption at the charge injection point (V_{GS} = +80V). As the lateral drain field is increased, charges flow from the source to drain and the current increases. At the same time, however, the strength of the gate field also decreases as the drain is approached, where the potential is $V_{GD} = V_{GS} - V_{DS}$.

As x increases, we see a systematic decrease in the strength of the electron polaron absorption until an electrically neutral point of zero potential is reached close to the drain, near x = 150 μm. After this crossover point, the channel potential is now negative with respect to the gate, resulting in a negative electric field and an injection of holes. This is reflected by an increase in absorption due to the accumulation of mobile holes. At the end of the conduction channel, where the drain potential is V_{GD} = -40V, we find a moderate hole polaron absorption.

Gray dotted lines in Fig. 4.4a mark the peak frequency positions of the electron and hole polaron absorptions extracted from Fig. 4.3 (ω_e = 3981 cm^{-1}, ω_h = 3413 cm^{-1}). Figure 4.4b shows IR absorption curves representing selected spectral slices taken from the 3D plot in Fig. 4.4a (colored horizontal lines). The shaded color curves in Fig. 4.4b directly visualize the transition from electron polaron absorption (bue spectra) before the charge neutral point near x = 150 μm, to hole polaron absorption (red spectra) as the drain at x = 200 μm is approached. We do observe small shifts in polaron peak frequencies, compared to the electrostatically-doped device show in Fig. 4.3, however the distinction between electron and hole polarons is quite clear. We have repeated these experiments for other ambipolar biasing configurations, and the same charge carrier-crossover behavior was observed, with polaron peak positions in general agreement with

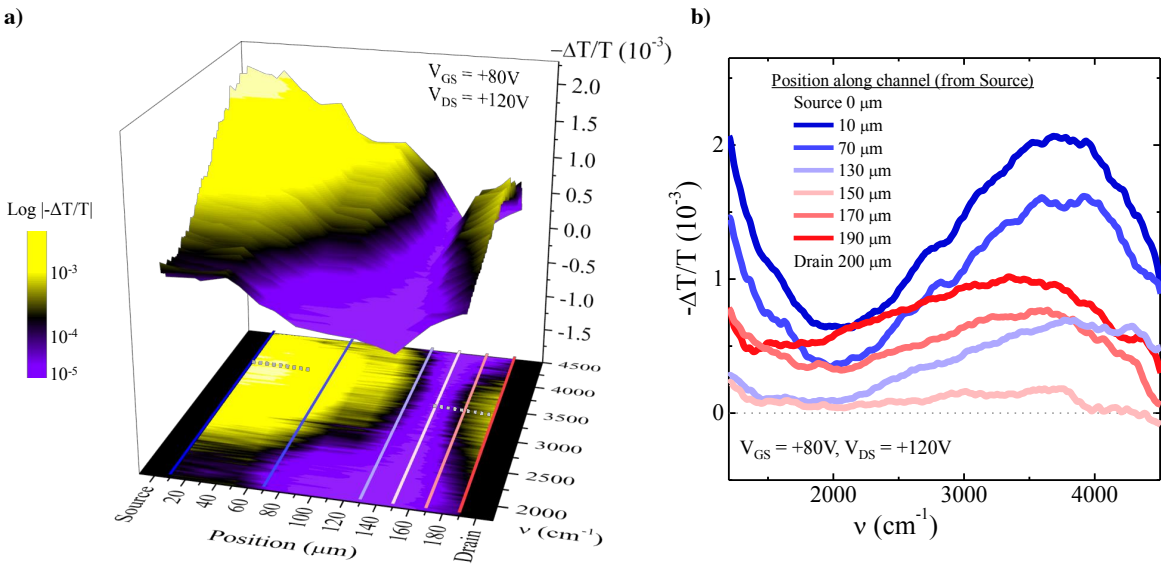

Figure 4.4: Representative IR microscopy data for a PDPPBBT device operating in the ambipolar regime with $V_{GS} = +80V$ and $V_{DS} = +120V$. a) 3D color plot visualizing the evolution of the polaronic absorption across the conduction channel. The IR beam size was reduced to 20 μm and scanned across the channel from the source electrode (x = 0 μm) to the drain (x = 200 μm). We find a prominent electron polaron absorption near the source gradually decrease in strength, and eventually transition to a weaker hole polaron absorption at the drain. A 2D colormap projection at the base of the graph shows the intensity of the IR response on a log scale, while colored lines indicate selected spectral slices. Gray dotted lines near the source and drain indicate peak frequency positions of electron and hole polarons, respectively. b) Selected IR absorption curves for specific positions in (a), showing the clear distinction between electron (blue) and hole polarons (red).

absorption spectra in Fig. 4.3.

4.3.4 Carrier density map for both unipolar and ambipolar operation

From the strength of the polaron absorption, we can quantify the accumulation of mobile carriers in the transistor channel. Conventionally, the optical functions of a material are connected to the density of charges via the frequency sum rule:[67]

$$\int_0^\infty \frac{nc}{4\pi}\alpha(\nu)d\nu \propto \frac{N_e}{m_{eff}}. \tag{4.2}$$

We define a similar quantity N_{eff} proportional to the density of injected electrons or holes as

$$N_{eff} = \int_{Pol} -\frac{\Delta T}{T}(\nu)d\nu. \tag{4.3}$$

The differential spectra are integrated only over the broad polaron absorptions from 2000 - 5000 cm^{-1}

Having established a quantitative measure of field-induced IR absorption, we connect the strength of this resonance directly to the number of charges, which can be independently calculated either by assuming a simple capacitative model:

$$n_{2D} = \frac{\kappa\epsilon_0}{eL}V_{GS} \tag{4.4}$$

or also by measuring transient charging currents, and thus calculating the total number of injected charges. The obtained doping-induced carrier density n_{2D} can then be correlated to the integrated intensity of the polaron absorption N_{eff}. We have previously shown this approach to be consistent with the linear capacitor model of an OFET.[84,108]

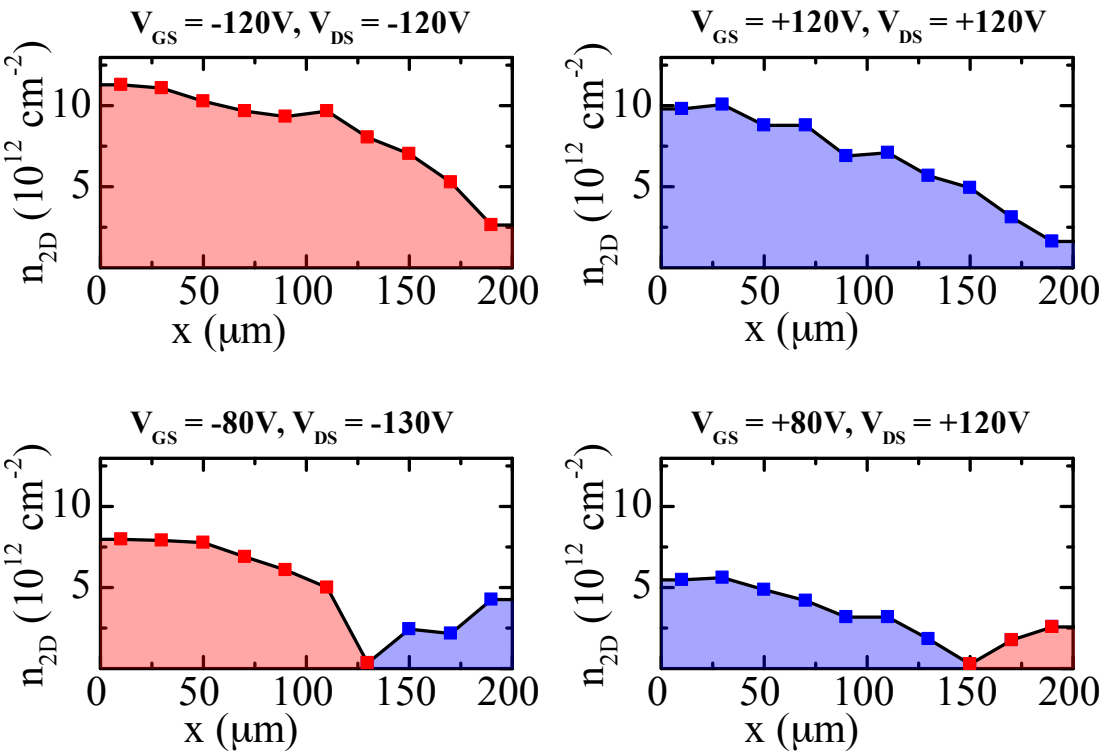

Figure 4.5: Charge density map across the conduction channel for a) unipolar hole, b) unipolar electron, and c), d) ambipolar OFET device operation. Areas under the curve are filled in with the color indicating the carrier type (red:holes, blue:electrons). The 2D charge density n_{2D} was extracted by comparing the integrated polaron absorption N_{eff}^{Pol} at each location to that obtained from the electrostatically-doped configuration in Fig. 4.3, and assuming linear device operation (Top inset in Fig. 4.3), typically valid for SiO2-based OFETs.[108]

We performed similar IR microscopy for four biasing regimes. Figure 4.5 shows a spatial map of the carrier density n_{2D} throughout the transistor channel, extracted from the totality of spectroscopic data for the respective gate and drain voltage configurations. The color of the shaded areas indicates the carrier type (red:holes, blue:electrons). For unipolar hole and electron operation (Fig. 4.5a and 4.5b respectively), we find a slow but steady suppresion of the polaron absorption from the source to the drain electrode, where the charge density is pinched off.

During ambipolar device operation (Fig. 4.5c and 4.5d), there exist spatially-separated hole-rich and electron-rich regions in the transistor channel, indicated by the red (p) and blue (n) shaded areas. The size of these regions, as well as position of the electron-hole boundary is determined by both the point of zero drain potential and the threshold voltage V_{th}.

These data confirm the well-established notion that the charge density in the saturation regime of an OFET is highly nonuniform, which comes directly from the conventional equations for field-effect transistors.[24] However, very few studies have directly imaged this behavior using IR spectroscopy,[112] and to our knowledge such spatiospectral mapping has never been demonstrated for an ambipolar organic system in the IR range. Since the saturation regime is most often invoked to estimate carrier mobility, a detailed account of the carrier distribution in the conduction channel, as well as the microscopic details provided by the spectroscopic features, is very useful for developing accurate models of OFET transport. This is especially important for ambipolar and light-emitting devices, where there is electron/hole coexistence in the transistor channel, as well as potentially important intrinsic differences between positive and negative charge carriers, as we have shown.

4.4 Summary

In summary, we have performed a systematic IR investigation of ambipolar charge injection in a small bandgap DA copolymer PDPPBBT. We register distinct absorptions associated with negative and positive polarons, and uncover

an intrinsic electron/hole asymmetry in the electronic structure of the DA system. Using diffraction-limited IR microscopy, we explored the evolution of the polaronic absorptions along the conducting channel of a functional PDPPBBT OFET, biased in both unipolar and ambipolar operating modes. In the ambipolar regime, we observe a spatial transition from hole to electron polaron absorption, indicating a coexistence of both charge carriers in the transistor channel akin to a pn junction diode.[113] Lastly, from the strength of the polaronic response, we constructed a spatial map of the charge carrier density from the source to the drain electrode in the various biasing regimes. Thus, we have demonstrated that IR microscopy combined with electrical transport measurements provide a comprehensive experimental approach with access to important details of the electronic structure, as well as a real-space charge density profile of functional transistor devices. This allows for a much more thorough and accurate characterization and modelling of transport behavior in organic semiconductors, especially ambipolar polymer systems.

4.5 Acknowledgements

Chapter 4, in part, has been submitted for publication of material as it may appear in O. Khatib, A. S. Mueller, H. T. Stinson, J. D. Yuen, A. J. Heeger, D. N. Basov, "Electron and hole polaron accumulation in low bandgap ambipolar donor-acceptor polymer transistors imaged by infrared microscopy", to Physical Review B. The dissertation author was the primary investigator and author of this work. caption[]

Chapter 5

Scattering scanning near-field optical microscopy (s-SNOM) of biological materials in aqueous media

Scattering scanning near-field optical microscopy (s-SNOM) has emerged as a useful tool capable of characterizing individual biomolecules and molecular materials. However, applications of scattering-based near-field techniques to real systems in biology has been hindered by a fundamental incompatibility between typical implementations of s-SNOM, and the aqueous environment required by many biological specimens. In this work, we propose a new infrared-suitable liquid cell architecture, enabling near-field imaging and nano-spectroscopy measurements by taking advantage of the unique properties of graphene. Large-area graphene acts as an impermeable monolayer lid that allows for nano-IR interrogation of the underlying molecular materials in liquid. Here we use s-SNOM to investigate tobacco mosaic virus (TMV) aggregates trapped with water underneath graphene. We are able to resolve individual viruses through graphene in near-field amplitude and phase images, and register the amide I and II bands of TMV using nanoscale fourier transform infrared spectroscopy (nano-FTIR). We verify the presence of

water in the graphene liquid cell by spectrally identifying the water absorption in the SNOM repsonse, amidst a large background contribution from the substrate. Our work paves the way for future studies using scattering-based near-field IR spectroscopy on biological systems in aqueous media.

5.1 Introduction

In biological and life sciences, fourier transform infrared (FTIR) spectroscopy serves as a ubiquitous noninvasive probe of vibrational fingerprints used to identify chemical and molecular species.[114] Small changes in the frequency and lineshape of conformational absorption modes of specific proteins can be used to characterize cells and tissues linked to diseases such as Alzheimer's[115] and cancer (Fig. 5.1).[114,116] However, due to the small IR absorption cross-section of individual proteins and molecules ($\sim 10^{-24}$ cm^2), large aggregates are needed to resolve the weak spectral features associated with biological systems.[117] Additionally, strong absorption from the vibrational and rotational modes of liquid water presents a large undesirable background, requiring substitution of either different isotopes of water, or specially prepared buffer solutions. Further, the long wavelength of IR light and consequently the coarse spatial resolution imposed by diffraction provide only an average response, potentially masking important heterogeneities associated with individual biomolecules. Figure 5.1 shows a comparison between the natural length scales of various biological materials, and the wavelength of IR probes used to study vibrational fingerprint absorptions.

Scattering scanning near-field optical microscopy (s-SNOM) circumvents the diffraction limit by combining an atomic force microscope (AFM) with coherent infrared lasers.[118,119] Incident light illuminates the sharp conducting tip in the vicinity of a sample. Scattered light from the coupled tip-sample system is detected in the far field, encoding dielectric information from the local near-field interaction. The incident field is highly confined to the tip apex, resulting in an infrared or optical probe with spatial resolution limited only by the tip diameter and not the wavelength of light. Various interferometric detection schemes can be employed

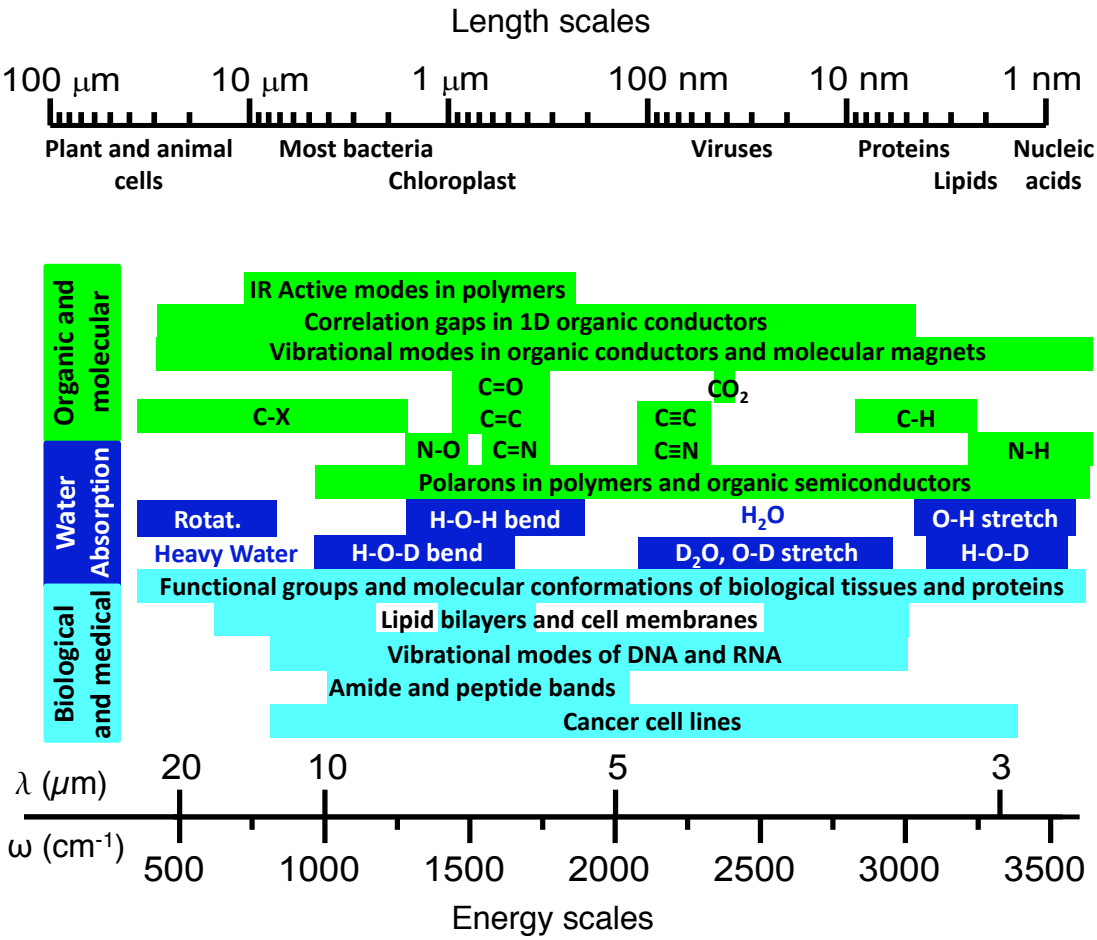

Figure 5.1: Top: Natural length scales for organisms and molecular materials in biology and life sciences. Bottom: Important IR absorptions and spectral fingerprints for various organic, biological, and chemical species accessible with fourier transform infrared spectroscopy (FTIR).

to extract both amplitude and phase of the near-field response from the scattered signal.[120] Coupling s-SNOM to monochromatic light allows for the construction of near-field images, while use of a broadband coherent source enables nanoscale fourier-transform infrared spectroscopy (nano-FTIR).[121,122,123]

Infrared nano-imaging[124] and nano-spectroscopy[125] have already demonstrated the ability to resolve individual biomolecules and chemically identify specific proteins.[126] However, widespread application of apertureless near-field spectroscopy in biology has been slowed by the incompatibility between physiological

conditions required for most living biological specimens, and typical implementations of s-SNOM. Specifically, the native aqueous environment of most biological samples prohibits the use of scattering tip-based optical probes in the infrared energy range, due to absorptive losses from the liquid medium. Measurement in water is a precondition for studying living systems, and is thus a necessary obstacle to overcome in order to apply rapidly-advancing nanoscale infrared techniques. There has been considerable development of aperture-based SNOM in the visible range.[127,128,129,130,131,132,133,134,135,136,137] However, these measurements require chemical modification to detect fluorescence, and in practice aperture-based probes are limited to a spatial resolution of 40-50nm, a factor of four worse than what is possible with scattering-based detection.[117] Although it is possible to measure local fields of materials in liquids with aperture SNOM, the experiments require specially designed AFM heads immersed in a liquid cell.

Here we propose an IR-compatible liquid cell architecture, enabling near-field imaging and spectroscopy measurements by taking advantage of the unique properties of graphene. Recent work has demonstrated the ability to trap liquids beneath graphene,[138,139,140] an atomically thin sheet of carbon atoms with remarkable mechanical, electrical, and IR properties.[141,142] Different graphene-based liquid cell architectures have already enabled nano-scale studies of biomaterials using high-resolution probes such as scanning tunneling microscopy[139] (STM) and transmission electron microscopy[143] (TEM). The IR transparency of graphene allows for extending such studies to scattering-based near-field techniques. In this work, we use s-SNOM to investigate tobacco mosaic viruses (TMV), a prototypical biological system, trapped with water underneath graphene.[144] The large-area graphene acts as an impermeable monolayer lid that allows for nano-IR interrogation of the underlying molecular materials in an aqueous environment. We are able to resolve individual viruses through graphene, and observe anticipated contrast in near-field amplitude and phase images. Further, we register spectroscopic resonances specific to TMV while encapsulated in the liquid cell. Our work paves the way for future studies using scattering-based near-field IR spectroscopy on biological systems in aqueous media.

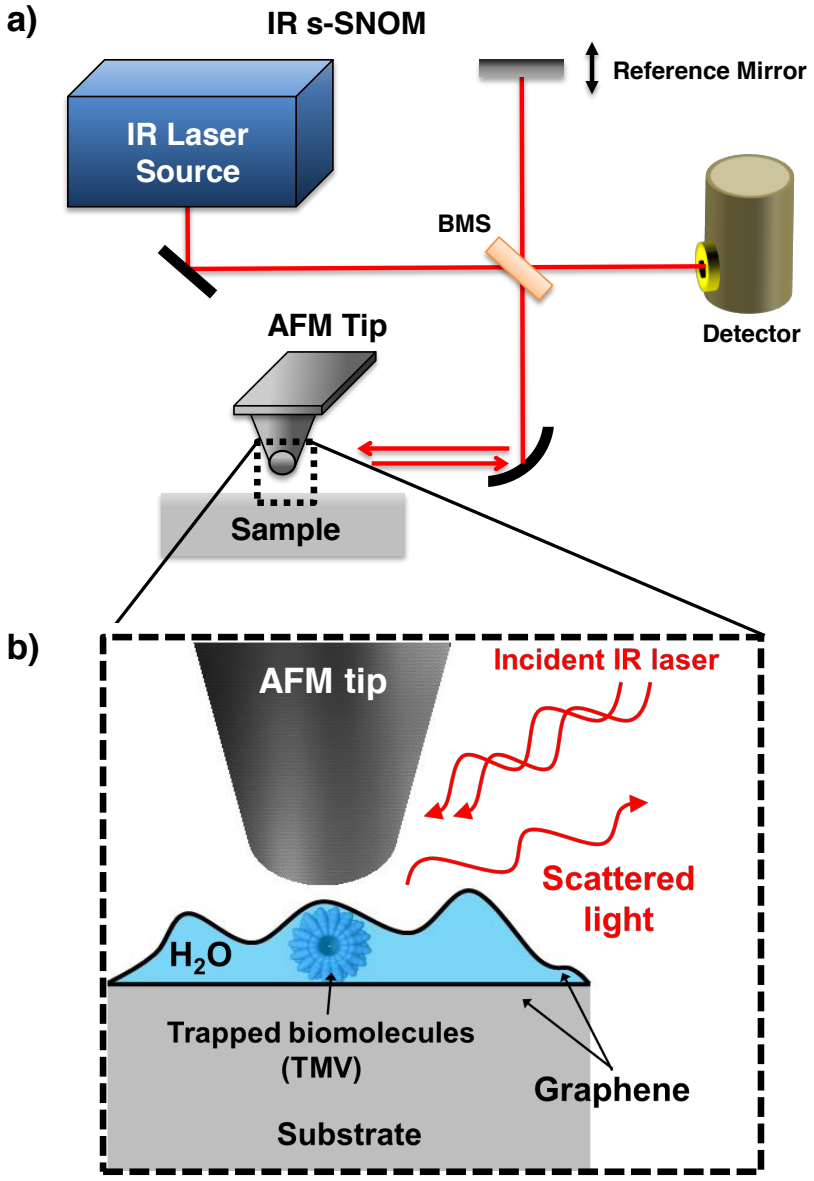

Figure 5.2: s-SNOM experimental setup with an IR-compatible graphene liquid cell. a) Schematic of scattering-based near-field IR imaging and spectroscopy apparatus. A continuous wave laser (CO_2 or quantum cascade) is used for our single frequency nano-imaging experiments in a pseudoheterdyne detection scheme with the reference mirror oscillating at 300 Hz. For nano-FTIR, coherent broadband mid-IR light from difference frequency generation (DFG) is utilized in an asymmetric Michelson configuration, where one arm of the interferometer is the scattered signal from the AFM tip. b) Zoomed-in representation of the tip-sample interaction, showing the geometry of the biomolecules in water trapped beneath a large area CVD graphene sheet in a liquid cell that allows for s-SNOM measurements.

5.2 Experimental details

5.2.1 Graphene liquid cell

Large-area graphene is grown from chemical vapor deposition (CVD) atop Cu foils. A lower methane-to-hydrogen ratio is used to give higher monolayer coverage. The method for trapping water with biomolecules beneath graphene is a wet transfer similar to what has been established previously for water alone.[139,144] The graphene is transfered with poly(methyl methacrylate) (PMMA) onto either mica or SiO_2/Si substrates. Successive deionized (DI) water baths clean the graphene films from residual etchant contamination after the transfer process. The samples are heated at 60° C for 5 minutes to drive out excess water and increase the graphene adhesion to the substrate. Remaining water from the wet transfer process is then trapped between the graphene overlayer and the underlying substrate surface. For SiO_2/Si substrates, an additional bottom layer of graphene was required for adequate adhesion, creating a graphene nano-sandwich. Both mica and SiO_2-based substrates function as suitable s-SNOM compatible liquid cells based on a graphene 'lid' as shown in Figure 5.2b.

5.2.2 s-SNOM setup

A schematic of the s-SNOM experimental setup is shown in Figure 5.2. For s-SNOM imaging and nano-FTIR measurements, we used a commercial near-field microscope (Neaspec GmbH, Germany) based on an AFM operating in tapping mode at a frequency $\Omega \sim 250$ kHz, with PtIr-coated cantilevers of nominal tip radius 20-30nm (Arrow NCPt, NanoWorld AG). The single frequency IR nano-imaging results we report in this work consisted of tip illumination by a CO_2 laser (Access Laser Company) with frequency $\omega = 890$ cm^{-1} (Fig. 5.2a). The scattered light from the tip is focused onto an HgCdTe detector (Kolmar Technologies). The detector signal, a combination of the local near-field interaction and a far-field background, is modulated by the oscillating AFM tip. The far-field background is strongly suppressed by demodulating the s-SNOM signal at higher order harmonics of the tip tapping frequency.[145] From the n-th harmonic of the scattered near-field

radiation $S_n(\omega) = |S_n|e^{i\phi_n}$, we recover both amplitude $|S_n|$ and phase ϕ_n of the field by employing a pseudoheterodyne detection scheme with a reference mirror that oscillates at 300Hz.[145]

For nano-FTIR experiments, we use a broadband laser source (Lasnix, Germany) based on difference-frequency generation (DFG).[121] A train of ultrashort pulses is generated by the nonlinear mixing of a near-IR Er-based fiber laser and a tunable IR supercontinuum laser (Toptica Photonics, Germany) inside a GaSe crystal.[146] The generated coherent broadband mid-infrared radiation is tunable from 650-2200 cm^{-1}, while for a given tuning range the full width at half maximum (FWHM) of the frequency spectrum is roughly 250-300 cm^{-1}. An asymmetric Michelson interfometer was used to analyze the s-SNOM signal, with the reference arm consisting of a step-scan mirror (1500 μm travel range). For nano-FTIR measurements, a frequency spectrum is collected in 60s with 8 cm $^{-1}$ resolution. Spectra are normalized to the s-SNOM spectrum from a gold reference.

5.3 Results and discussion

5.3.1 IR nano-imaging of TMV in graphene liquid cell on mica substrate

Figure 5.3a shows a large-area AFM scan of TMV viruses contained in a graphene liquid cell on mica. The TMV are typically identified directly from the AFM topography through a well defined rod-shaped structure, with a length of 300 nm and a diameter of 18 nm.[147,148,124] When contained in a graphene-based cell with water, however, the width and height of the TMV as registered by the AFM tip are modified by the graphene overlayer, which conforms to the shape of the virus and surrounding water. Thus the 300nm virus length was used to discern the TMV from the environment. In addition to virus aggregates, we observe many large-scale features associated with residue and contaminants from either the tobacco plant, or the CVD graphene overlayer, which often contains many wrinkles and folds.[149]

Acquired concurrently with topography are the s-SNOM amplitude and

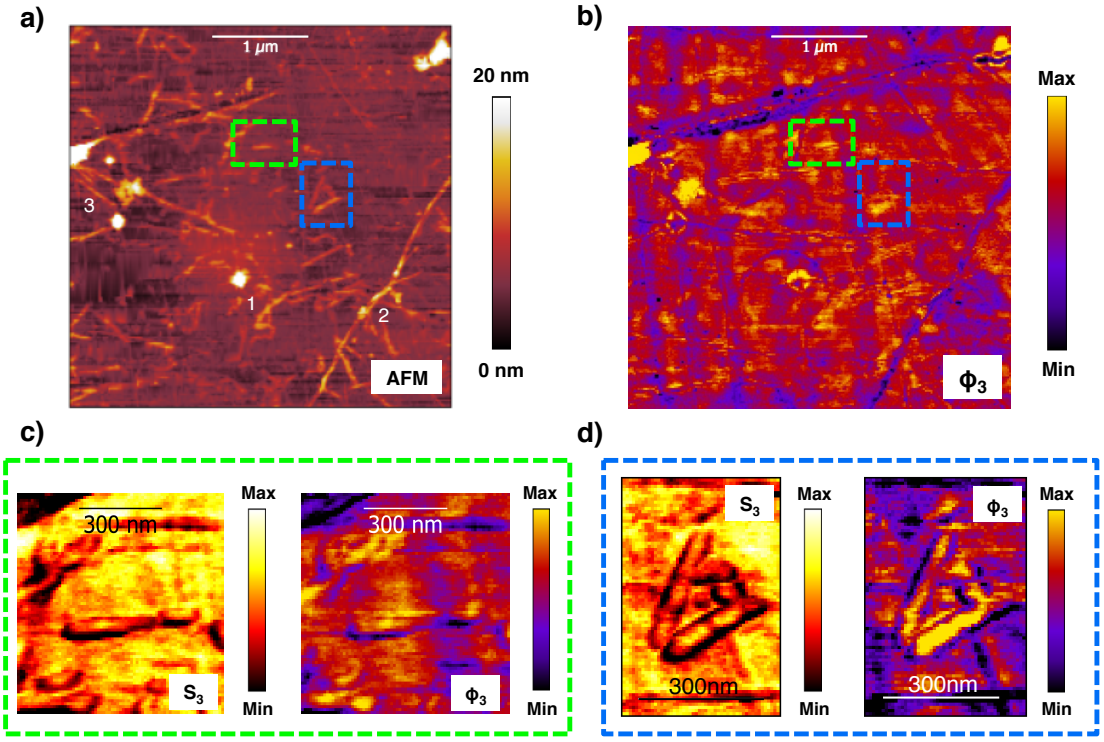

Figure 5.3: a) Large area 4x4μm^2 AFM topography scan of IR-compatible graphene liquid cell on a mica substrate. Large-scale morphological features accompanying the presence of TMV aggregates include additional tobacco plant material (1), graphene folds/wrinkles (2), and possible PMMA residue (3). b) Third harmonic of the phase of the scattered near-field signal ϕ_3, defined in the main text. Green (c) and blue (d) boxed regions in the large-area topography and phase scans are high-reslolution nano-IR images of the third harmonic of the near-field amplitude S_3 (left panel) and phase ϕ_3 (right panel). Individual viruses are easily identified through the graphene top layer from the near-field contrast observed in both amplitude and phase. Nano-IR images were acquired using a CO_2 laser (ω = 890 cm^{-1}).

phase images using a CO_2 laser with $\omega = 890$ cm^{-1}. Figure 5.3b shows the third harmonic of the scattered near-field phase ϕ_3. We register near-field contrast in the locations of the TMV, highlighted by the green and blue color boxes in Fig. 5.3a and 5.3b, as well as many features in the phase image occurring near areas with much residue or wrinkles in the graphene sheet (number labels in Fig. 5.3a). Additionally, we observe a vertical stripe pattern that could indicate varying amounts of water. Nano-confined water has been shown to form filaments and conform to the templated CVD graphene morphology.[144]

High-reslolution nano-IR images for isolated TMV (colored boxes in Fig. 5.3a) are shown in Fig. 5.3c and 5.3d, with a pixel size of 10nm, corresponding to the resolution limited by the tip radius. The third harmonic of the scattering near-field amplitude and phase are shown in the left and right panels, respectively. We observe significant s-SNOM contrast in regions with TMV. While optical contrast in the scattering amplitude alone can sometimes be trivially attributed to a topographical effect, phase shifts are less susceptible to such artifacts and in principle more sensitive to electronic effects and vibrational absorptions.[150] In addition, higher harmonics of the scattered signal are progressively less sensitive to topographical artifacts by virtue of the highly nonlinear tip-sample near-field interaction. We discuss the origin of the near-field contrast surrounding the TMV below.

5.3.2 Nano-FTIR absorption for TMV in graphene liquid cell on SiO_2 substrate

Through the outer graphene layer, an IR-transparent conductor, we are able to image individual biomolecules surrounded by water. In addition to single-frequency imaging, we performed nano-FTIR of TMV and the local aqueous environment. Figure 5.4a shows the AFM topography of a single virus in a graphene liquid cell on a SiO_2 substrate. We performed a nano-FTIR linescan across the TMV, with a tracjectory shown by the green dotted line in Fig. 5.4a, collecting a spectrum at each pixel in steps of 20nm as the tip is scanned across the sample. The broadband DFG laser source was tuned to the frequency range 1400-1800

cm^{-1}, where we expect absorption from the amide I (1660 cm^{-1}) and II (1550 cm^{-1}) bands in TMV,[125] as well as the bending mode in liquid water ν_{H_2O} (1640 cm^{-1}), as shown in Figure 5.1.[151] For the nano-spectroscopy measurements, we chose graphene liquid cells based on SiO_2 because intrinsic vibrational modes from the mica substrate dominate this frequency region where both water and TMV absorb.[152]

Nano-FTIR absorption spectra for a liquid cell containing TMV are shown in Figure 5.4b. For weaker resonances, the near-field absorption is approximated by plotting only the imaginary part of the scattered s-SNOM signal, $\mathrm{Im}[S_n e^{i\phi_n}] = S_n sin(\phi_n)$, which has been shown to correlate well with far-field absorption spectra.[150] Data shown in Fig. 5.4b have been normalized to the signal from a spectrally flat gold reference. The black curve in Fig. 5.4b shows nano-FTIR spectra for TMV averaged over the green dotted line in Fig. 5.4a. We observe two small spectral features at 1520 cm^{-1} and 1660 cm^{-1} superimposed on what appears to be the tail of a broad absorption background. The blue curve represents nano-FTIR spectra for a region away from the virus, where the salient feature is a minimum in the data near 1610 cm^{-1}.

In order to understand the nano-imaging and spectroscopy data, it is instructive to more closely examine the microscopic tip-sample interaction. Contrast in the near-field images is indicative of a change in the dielectric environment of the tip apex, often due to strong resonances in the sample leading to significant phase shifts and enhancements of the scattered light.[153] The evanescent fields emitted from the photoexcited tip apex can penetrate well beneath the sample surface.[154] Consequently, the complete sample response includes contributions from underlying layers.

While the spatial resolution of s-SNOM is ultimately limited by the diameter of the tip apex, the in-plane resolution and probing depth are not the same. In practice, the depth of s-SNOM is effectively several tens of nanometers.[155] Thus the tip-sample interaction includes biomolecules, water, graphene, and the underlying substrate. As a result there are many sources of variations in the scattered near-field signal due to significant inhomogeneity in these various layers. The im-

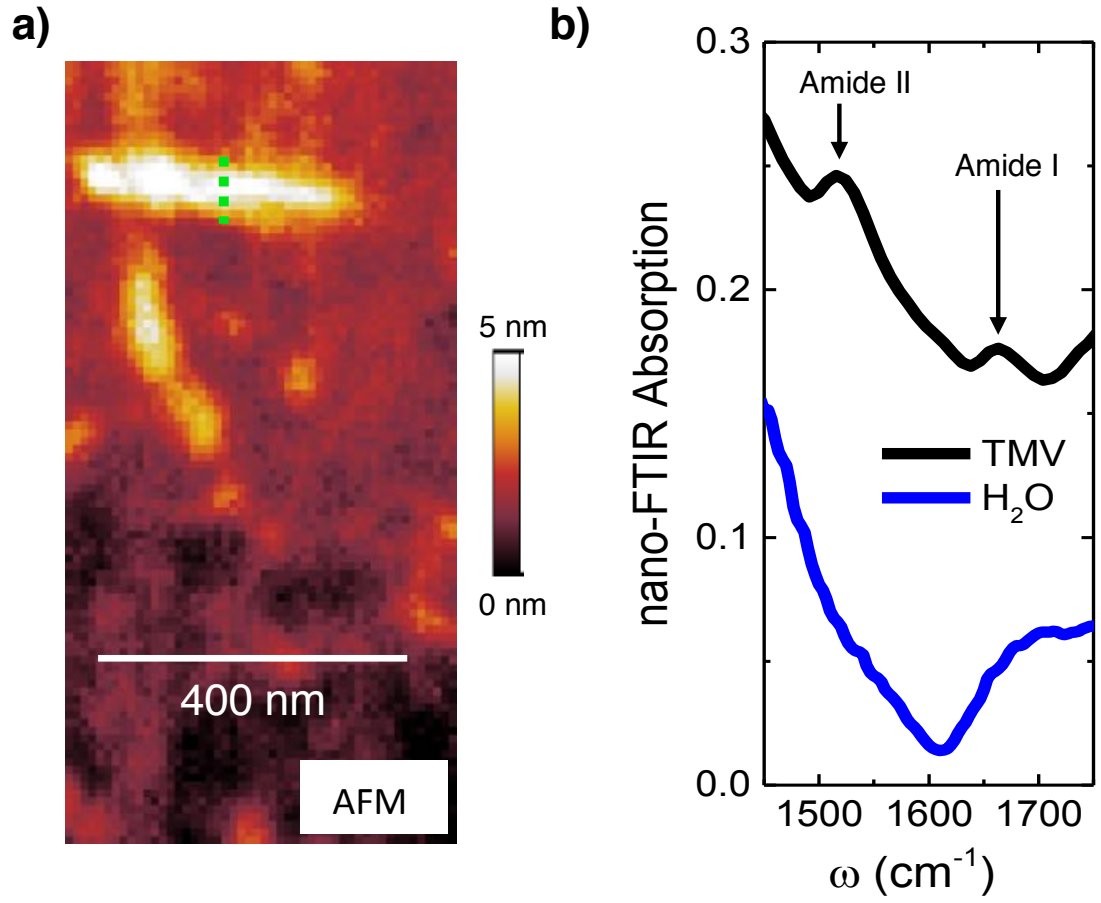

Figure 5.4: (a) AFM topography and (b) nano-FTIR absorption spectra for TMV in a graphene liquid cell on a SiO_2 substrate. Absorption spectra are plotted in the range 1450-1750 cm^{-1} and computed from the second harmonic of the scattered near-field signal $S_2(\omega)$, with an acquisition time of 60s per spectrum and 8 cm^{-1} resolution. All spectra are normalized to Au. The green dotted line in (a) indicates the trajectory of AFM tip during the nano-FTIR linescan over the TMV. The nano-FTIR absorption spectra for TMV (black curve) in (b) is averaged over this AFM linescan. The blue curve in (b) is an absorption spectrum of the graphene liquid cell away from the TMV. The prominent spectral feature associated with the presence of water in the liquid cell is a minimum in the s-SNOM signal near 1610 cm^{-1}, as detailed in the text.

ages in Fig. 5.3 were acquired using a CO_2 laser (ω = 890 cm^{-1}) in a frequency range where there is likely considerable absorption from water,[156] mica,[152,157] and SiO_2.[158]

Nano-FTIR spectra in Fig. 5.4b for the graphene liquid cell on SiO_2 (blue curve) exhibit a prominent feature near 1610 cm^{-1}. Bulk liquid water posseses a sharp vibrational absorption at 1640 cm^{-1} due to the H-O-H bend mode ν_{H_2O} (Fig. 5.1).[151] We can understand the evolution of the nano-FTIR absorption spectra by considering the effect of the graphene layers and the oxide. During the growth process, it is highly likely that the large-area graphene becomes doped from atmospheric adsorbates or PMMA residue. Although intrinsically IR-transparent, the free carriers in graphene can interact with phonons in the underlying SiO_2 oxide by a plasmon-phonon coupling.[159] This coupling results in a significant enhancement and broadening of the near-field response near the optical phonon of SiO_2 (1100-1200 cm^{-1}). At high enough doping, the frequency position of sharp resonances can shift as well. The unintentional doping of graphene can be non-uniform throughout a single large-area CVD sheet.[149]

5.3.3 Modeling s-SNOM response of graphene cell

To simulate the s-SNOM response of the entire multilayer system of the cell, we employed the recently-developed *Lightning Rod Model*: a quantitative model of the near-field interaction that goes beyond simplistic approximations of the tip-sample system, and utilizes a realistic probe geometry as well as electrodynamical effects.[160] Figure 5.5b shows a schematic of the subsequent layers constituting the graphene liquid cell. For the simulations, we used tabulated H_2O and SiO_2 optical constants taken from the literature.[156,158] For the top and bottom graphene layers, we assume a moderate doping level denoted by the chemical potential, with μ = 2000 cm^{-1}, and use the dielectric function calculated within the random phase approximation (RPA) method.[159]

Figure 5.5a shows a simulated s-SNOM spectrum predicted by the *Lightning Rod Model* for a graphene liquid cell consisting of 10nm of water sandwiched between two sheets of doped graphene on silicon oxide (blue line). Also included

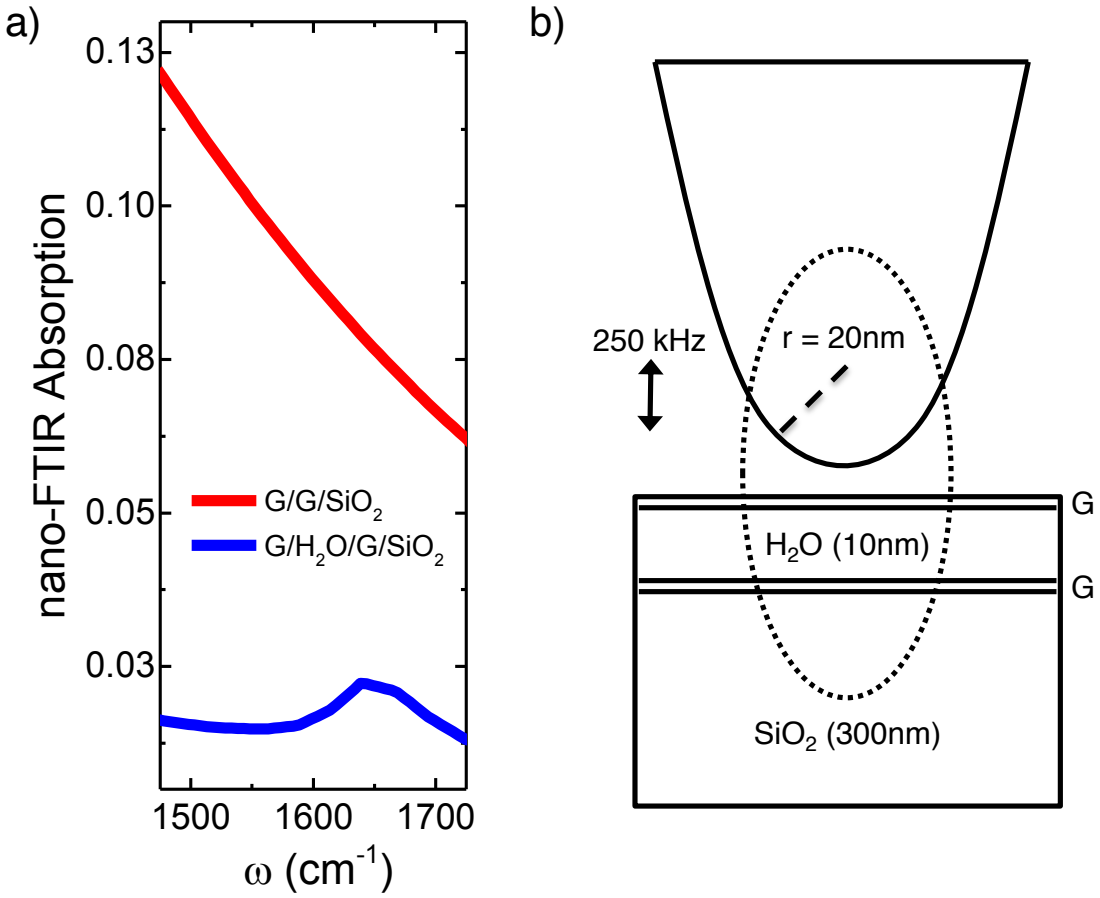

Figure 5.5: a) s-SNOM simulation of nano-FTIR absorption spectra for a graphene liquid cell on a SiO_2 substrate with (blue curve) and without (red curve) a small layer of water. The presence of water in the cell significantly modifies the total s-SNOM response. b) Schematic of multilayer model (detailed in text) used to simulate the near-field response of the graphene liquid cell.

for comparison is the spectrum calculated in the absence of water (red line in Fig. 5.5a). The significant graphene enhancement of the SiO_2 phonon results in a large background in the s-SNOM response. However, the presence of water significally modifies the predicted nano-FTIR absorption, and results in a spectral behavior similar to what we observe experimentally in the nano-FTIR data (blue line in Fig. 5.4b). Without any liquid, the spectra evolve smoothly and monotonically, shown by the red curve in Fig. 5.5a. We observe a slight deviation of the lineshape and center frequency of the water absorption from the simulated s-SNOM response. However, this is not surprising considering that bulk liquid H_2O optical constants were used in the model, which may not accurately reflect potential differences in the infrared response of interfacial and nano-confined water. Despite interference from the substrate, we are able to verify the presence of a layer of water in the graphene cell. Furthermore, we are sensitive to the very small amount of trapped water (likely 5-15 nm) amidst several other absorbing materials, enabling further more detailed studies on other biomolecules of comparable size (< 20nm), using a similar graphene liquid cell architecture.

In addition to absorption from water, we expected to observe spectral features associated with the amide bands in TMV, which also occur in our experimental frequency range.[125] The nano-FTIR absorption data for TMV in Fig. 5.4b clearly show two weak resonances at 1520 cm^{-1} and 1660 cm^{-1} indicative of the amide II and I bands, respectively, superimposed on the broad s-SNOM response from the graphene-SiO_2 subsystem. While the frequency position of the amide I bands agrees very well with what has been previously observed in nano-FTIR,[125] the amide II absorption is considerably redshifted compared to the expected resonance near 1550 cm^{-1}. At these lower energies there is a stronger s-SNOM contribution from the SiO_2 phonon and doped graphene, which is likely responsible for such a spectral shift of the much weaker absorption mode in the TMV.

As mentioned previously, sandwiched TMV samples on SiO_2 were more suitable for nano-spectroscopy measurements due to the lack of vibrational absorptions associated with the substrate in the frequency range of interest. Conversely, mica substrates were used for nano-IR imaging experiments because of plasmonic inter-

ference effects observed in doped graphene on SiO_2 with a CO_2 laser.[161] To realize the full potential of s-SNOM imaging and spectroscopy for quantitative characterization of biomolecules in aqueous media, the liquid cell architecture can be optimized by selecting spectrally flat substrates such as Si, or by using free standing graphene nanosandwich cells transferred to TEM grids.[143] Additionally, future iterations of such graphene-based liquid cells could employ other isotopes of water involving varying mixtures of deuterium, effectively tuning the bending mode vibration out of the frequency range of interest.[151] Lastly, besides graphene, other 2D materials can be explored for use as a nanofluidic lid, such as boron nitride (BN), silicon nitride (Si_3N_4), or transition metal dichalcogenides (TMDCs).

5.4 Conclusion

To summarize, we have performed s-SNOM on TMV aggregates trapped, together with water, underneath large-area monolayer graphene. We are able to image individual viruses through graphene, registering significant contrast in both amplitude and phase of the scattered near-field signal. The presence of water in the liquid cells was confirmed using nano-FTIR spectroscopy. We observed in the near-field response spectral features associated with trapped water, amidst a large background contribution from the underlying silicon oxide substrate. Further, we are able to measure weak absorptions associated with the amide bands in TMV inside the graphene liquid cell. Our nano-spectroscopic probe is able to register as little as a 10 nm layer of water, enabling studies of other macromolecular materials using a similar sample architecture. We have demonstrated that scattering-based near-field techniques are applicable to biomolecules in aqueous media. Our work sets the stage for further nano-IR studies of biological and molecular materials utilizing optimized liquid cells employing ultrathin lids made of graphene and other 2D nano-materials.

5.5 Acknowledgements

Nano-spectroscopy work at UCSD is supported by the Office of Naval Research (ONR). This work is being prepared for publication of material as it may appear in O. Khatib, J. D. Wood, A. S. McLeod, M. Goldflam, M. Wagner, J. W. Lyding, D. N. Basov, "Graphene-based platform for nano-scale infrared near-field nano-spectroscopy of biological substances in aqueous media". The dissertation author is the primary investigator and author of this work.

Bibliography

[1] Heeger, A., Kivelson, S., Schrieffer, J., and Su, W. *Reviews of Modern Physics* **60**(3), 781–851 (1988).

[2] McCullough, R. D. *Advanced Materials* **10**(2), 93–116 January (1998).

[3] Panzer, M. and Frisbie, C. *Advanced Functional Materials* **16**(8), 1051–1056 May (2006).

[4] Yang, H., LeFevre, S. W., Ryu, C. Y., and Bao, Z. *Applied Physics Letters* **90**(17), 172116 (2007).

[5] Ahn, C. H., Triscone, J.-M., and Mannhart, J. *Nature* **424**(6952), 1015–8 August (2003).

[6] Ahn, C., Bhattacharya, A., and Ventra, M. D. *Reviews of Modern ...* **78**(December), 1185–1212 (2006).

[7] Brocks, G., van den Brink, J., and Morpurgo, A. *Physical Review Letters* **93**(14), 1–4 September (2004).

[8] Dhoot, A. S., Yuen, J. D., Heeney, M., McCulloch, I., Moses, D., and Heeger, A. J. *Proceedings of the National Academy of Sciences of the United States of America* **103**(32), 11834–7 August (2006).

[9] Yuen, J. D., Dhoot, A. S., Namdas, E. B., Coates, N. E., Heeney, M., McCulloch, I., Moses, D., and Heeger, A. J. *Journal of the American Chemical Society* **129**(46), 14367–71 November (2007).

[10] Panzer, M. J. and Frisbie, C. D. *Journal of the American Chemical Society* **129**(20), 6599–607 May (2007).

[11] Herlogsson, L., Noh, Y.-Y., Zhao, N., Crispin, X., Sirringhaus, H., and Berggren, M. *Advanced Materials* **20**(24), 4708–4713 December (2008).

[12] Mills, T., Kaake, L. G., and Zhu, X.-Y. *Applied Physics A* **95**(1), 291–296 December (2009).

[13] Kao, C. Y., Lee, B., Wielunski, L. S., Heeney, M., McCulloch, I., Garfunkel, E., Feldman, L. C., and Podzorov, V. *Advanced Functional Materials* **19**(12), 1906–1911 June (2009).

[14] Calhoun, M. F., Sanchez, J., Olaya, D., Gershenson, M. E., and Podzorov, V. *Nature materials* **7**(1), 84–9 January (2008).

[15] Pope, M. and Swenberg, C. E. *Electronic Processes in Organic Crystals and Polymers*. Oxford University Press, New York, (1999).

[16] Li, Z. Q., Wang, G. M., Sai, N., Moses, D., Martin, M. C., Di Ventra, M., Heeger, a. J., and Basov, D. N. *Nano letters* **6**(2), 224–8 February (2006).

[17] Bao, Z., Dodabalapur, A., and Lovinger, A. J. *Applied Physics Letters* **69**(26), 4108 (1996).

[18] Sai, N., Li, Z. Q., Martin, M. C., Basov, D. N., and Di Ventra, M. *Physical Review B* **75**, 045307 January (2007).

[19] Bao, Z. and Locklin, J. *Organic field-effect transistors*. Taylor & Francis, Boca Raton, (2007).

[20] Assadi, A., Gustafsson, G., and Willander, M. *Synthetic Metals* **37**, 123–130 (1990).

[21] Brown, P. J., Sirringhaus, H., Harrison, M., Shkunov, M., and Friend, R. H. *Physical Review B* **63**(12), 125204 March (2001).

[22] Burgi, L., Friend, R. H., and Sirringhaus, H. *Applied Physics Letters* **82**(9), 1482 (2003).

[23] Dhoot, A. S., Wang, G. M., Moses, D., and Heeger, A. J. *Physical Review Letters* **96**(24), 246403 June (2006).

[24] Braga, D. and Horowitz, G. *Advanced Materials* **21**(14-15), 1473–1486 April (2009).

[25] Singh, T. B. and Sariciftci, N. S. *Annual Review of Materials Research* **36**(1), 199–230 August (2006).

[26] Li, Z., Podzorov, V., Sai, N., Martin, M., Gershenson, M., Di Ventra, M., and Basov, D. *Physical Review Letters* **99**(1), 016403 July (2007).

[27] Fischer, M., Dressel, M., Gompf, B., Tripathi, A. K., and Pflaum, J. *Applied Physics Letters* **89**(18), 182103 (2006).

[28] Lenk, T. J., Hallmark, V. M., Hoffmann, C. L., Rabolt, J. F., Castner, D. G., Erdelen, C., and Ringsdorf, H. *Langmuir* **10**(12), 4610–4617 December (1994).

[29] Tsao, M.-W., Hoffmann, C. L., Rabolt, J. F., Johnson, H. E., Castner, D. G., Erdelen, C., and Ringsdorf, H. *Langmuir* **13**(16), 4317–4322 August (1997).

[30] Sinapi, F., Issakova, T., Delhalle, J., and Mekhalif, Z. *Thin Solid Films* **515**(17), 6833–6843 June (2007).

[31] Jiang, X. M. and Österbacka, R. *Advanced Functional Materials* **12**, 587–597 (2002).

[32] Österbacka, R., Jiang, X., An, C., Horovitz, B., and Vardeny, Z. *Physical Review Letters* **88**(22), 226401 May (2002).

[33] Kim, Y. H. and Heeger, A. J. *Physical Review B* **40**(12), 8393–8398 (1989).

[34] Horovitz, B. *Solid State Communications* **41**(10), 729–734 March (1982).

[35] Horovitz, B., Österbacka, R., and Vardeny, Z. *Synthetic Metals* **141**(1-2), 179–183 March (2004).

[36] Österbacka, R., An, C. P., Jiang, X. M., and Vardeny, Z. V. *Science* **287**(5454), 839–42 February (2000).

[37] Kim, Y. H., Spiegel, D., Hotta, S., and Heeger, A. J. *Physical Review B* **38**, 5490–5495 (1988).

[38] Dressel, M. and Grüner, G. *Electrodynamics of Solids*. Cambridge University Press, Cambridge, (2002).

[39] Qazilbash, M., Brehm, M., Andreev, G., Frenzel, a., Ho, P.-C., Chae, B.-G., Kim, B.-J., Yun, S., Kim, H.-T., Balatsky, a., Shpyrko, O., Maple, M., Keilmann, F., and Basov, D. *Physical Review B* **79**(7), 075107 February (2009).

[40] Brazovskii, S. and Kirova, N. *JETP lett* **33**(1), 4–8 (1981).

[41] Sirringhaus, H., Brown, P. J., Friend, R. H., Nielsen, M. M., Bechgaard, K., and Spiering, A. J. H. *Nature* **401**, 685–688 (1999).

[42] Wohlgenannt, M., Jiang, X., and Vardeny, Z. *Physical Review B* **69**(24), 241204 June (2004).

[43] Cataudella, V., De Filippis, G., and Iadonisi, G. *The European Physical Journal B ...* **12**, 17–22 (1999).

[44] Ciuchi, S. and Fratini, S. *Physical Review B* **79**(3), 035113 January (2009).

[45] Lee, K., Cho, S., Park, S. H., Heeger, a. J., Lee, C.-W., and Lee, S.-H. *Nature* **441**(7089), 65–8 May (2006).

[46] Kelley, T. W., Baude, P. F., Gerlach, C., Ender, D. E., Muyres, D., Haase, M. a., Vogel, D. E., and Theiss, S. D. *Chemistry of Materials* **16**(23), 4413–4422 November (2004).

[47] Katz, H. E. and Huang, J. *Annual Review of Materials Research* **39**(1), 71–92 August (2009).

[48] Wang, S., Kappl, M., Liebewirth, I., Müller, M., Kirchhoff, K., Pisula, W., and Müllen, K. *Advanced materials* **24**(3), 417–20 January (2012).

[49] Klauk, H. *Chemical Society reviews* **39**(7), 2643–66 July (2010).

[50] Meijer, E. J., de Leeuw, D. M., Setayesh, S., van Veenendaal, E., Huisman, B. H., Blom, P. W. M., Hummelen, J. C., Scherf, U., Kadam, J., and Klapwijk, T. M. *Nature materials* **2**(10), 678–82 October (2003).

[51] Chen, Z., Lee, M. J., Shahid Ashraf, R., Gu, Y., Albert-Seifried, S., Meedom Nielsen, M., Schroeder, B., Anthopoulos, T. D., Heeney, M., McCulloch, I., and Sirringhaus, H. *Advanced materials* **24**(5), 647–52 February (2012).

[52] Cho, S., Lee, J., Tong, M., Seo, J. H., and Yang, C. *Advanced Functional Materials* **21**(10), 1910–1916 May (2011).

[53] Steckler, T. T., Zhang, X., Hwang, J., Honeyager, R., Ohira, S., Zhang, X.-h., Grant, A., Ellinger, S., Odom, S. A., Sweat, D., Tanner, D. B., Rinzler, A. G., Barlow, S., Bre, J.-l., Kippelen, B., Marder, S. R., and Reynolds, J. R. *Journal of the American Chemical Society* **131**, 2824–2826 (2009).

[54] DuBois, C. J., Abboud, K. A., and Reynolds, J. R. *The Journal of Physical Chemistry B* **108**, 8550–8557 (2004).

[55] Brédas, J. L. *J. Chem. Phys.* **82**, 3808–3811 (1985).

[56] Brédas, J. L., Heeger, A. J., and Wudl, F. *J. Chem. Phys.* **85**, 4673–4678 (1986).

[57] Ahmed, E., Subramaniyan, S., and Kim, F. *Macromolecules* **44**, 7207–7219 (2011).

[58] Yuen, J. D., Kumar, R., Zakhidov, D., Seifter, J., Lim, B., Heeger, A. J., and Wudl, F. *Advanced Materials* **23**, 3780–3785 July (2011).

[59] Zhang, X., Steckler, T. T., Dasari, R. R., Ohira, S., Potscavage, W. J., Tiwari, S. P., Coppée, S., Ellinger, S., Barlow, S., Brédas, J.-L., Kippelen, B., Reynolds, J. R., and Marder, S. R. *Journal of Materials Chemistry* **20**(1), 123 (2010).

[60] Yuen, J. D., Wang, M., Fan, J., Sherbla, D., Kemei, M., Scarongella, M., Valouch, S., Pho, T., Chestnut, E. C., Banerji, N., Bendikov, M., and Wudl, F. .

[61] Matsui, H. and Hasegawa, T. *Applied Physics Letters* **95**(22), 223301 (2009).

[62] Haas, S., Matsui, H., and Hasegawa, T. *Physical Review B* **82**, 161301 (2010).

[63] Ferlauto, A. and Ferreira, G. *Journal of Applied . . .* **92**(5), 2424–2436 (2002).

[64] van den Oever, P. J., van de Sanden, M. C. M., and Kessels, W. M. M. *Journal of Applied Physics* **101**(12), 123529 (2007).

[65] Smits, E. C. P., Anthopoulos, T. D., Setayesh, S., van Veenendaal, E., Coehoorn, R., Blom, P. W. M., de Boer, B., and de Leeuw, D. M. *Physical Review B* **73**(20), 205316 May (2006).

[66] Zaumseil, J. and Sirringhaus, H. *Chemical reviews* **107**(4), 1296–323 April (2007).

[67] Wooten, F. *Optical properties of solids*. Academic, New York, (1972).

[68] Ehrenfreund, E., Vardeny, Z., Brafman, O., and Horovitz, B. *Physical Review B* **36**(3), 1535–1553 (1987).

[69] Del Zoppo, M., Castiglioni, C., Zuliani, P., and Zerbi, G. *Handbook of Conducting Polymers*. Marcel Dekker, New York, 2nd edition, (1988).

[70] Gussoni, M., Castiglioni, C., and Zerbi, G. *Spectroscopy of Advanced Materials*. Wiley, New York, (1991).

[71] Ehrenfreund, E. and Vardeny, Z. *Proceedings of the IEEE* **3145**, 324–332 (1997).

[72] Girlando, A., Painelli, A., and Soos, Z. G. *The Journal of Chemical Physics* **98**(9), 7459 (1993).

[73] Neugebauer, H. *Journal of Electroanalytical Chemistry* **563**(1), 153–159 February (2004).

[74] Chen, Z., Bird, M., Lemaur, V., Radtke, G., Cornil, J., Heeney, M., McCulloch, I., and Sirringhaus, H. *Physical Review B* **84**(11), 115211 September (2011).

[75] Li, Z. Q., Henriksen, E. a., Jiang, Z., Hao, Z., Martin, M. C., Kim, P., Stormer, H. L., and Basov, D. N. *Nature Physics* **4**(7), 532–535 June (2008).

[76] Zhang, L., Li, Z., Basov, D., Fogler, M., Hao, Z., and Martin, M. *Physical Review B* **78**(23), 235408 December (2008).

[77] Li, Z., Henriksen, E., Jiang, Z., Hao, Z., Martin, M., Kim, P., Stormer, H., and Basov, D. *Physical Review Letters* **102**(3), 037403 January (2009).

[78] Zhang, Y., Tang, T.-T., Girit, C., Hao, Z., Martin, M. C., Zettl, A., Crommie, M. F., Shen, Y. R., and Wang, F. *Nature* **459**(7248), 820–3 June (2009).

[79] Horng, J., Chen, C., Geng, B., Girit, C., and Zhang, Y. *Physical Review B* **83**, 165113 (2011).

[80] Chapler, B. C., Mack, S., Ju, L., Elson, T. W., Boudouris, B. W., Namdas, E., Yuen, J. D., Heeger, a. J., Samarth, N., Di Ventra, M., Segalman, R. a., Awschalom, D. D., Wang, F., and Basov, D. N. *Physical Review B* **86**(16), 165302 October (2012).

[81] Sirringhaus, H. *Advanced Materials* **21**, 3859–3873 (2009).

[82] Salleo, A., Chen, T. W., Völkel, A. R., Wu, Y., Liu, P., Ong, B. S., and Street, R. A. *Physical Review B* **70**(11), 115311 September (2004).

[83] Lee, K. and Heeger, J. *Physical Review B* **48**(20), 14884–14891 (1993).

[84] Khatib, O., Lee, B., Yuen, J., Li, Z. Q., Di Ventra, M., Heeger, a. J., Podzorov, V., and Basov, D. N. *Journal of Applied Physics* **107**(12), 123702 (2010).

[85] Cravino, A., Neugebauer, H., Luzzati, S., Catellani, M., Petr, A., Dunsch, L., and Sariciftci, N. S. *The Journal of Physical Chemistry B* **106**(14), 3583–3591 April (2002).

[86] Neugebauer, H., Kvarnström, C., Cravino, A., Yohannes, T., and Sariciftci, N. S. *Synthetic metals* **116**, 115–121 (2001).

[87] Weiser, G. *physica status solidi (a)* **18**, 347–359 (1973).

[88] Phillips, S., Worland, R., Yu, G., and Hagler, T. *Physical Review B* **40**(14), 9751–9759 (1989).

[89] Campbell, I., Hagler, T., Smith, D., and Ferraris, J. *Physical review letters* **76**(11), 1900–1903 March (1996).

[90] Horvath, A., Weiser, G., Baker, G., and Etemad, S. *Physical Review B* **51**(5), 2751–2758 (1995).

[91] Sebastian, L., Weiser, G., and Bässler, H. *Chemical Physics* **61**, 447 (1981).

[92] Weiser, G. *Physical Review B* **45**(24), 14076–14085 (1992).

[93] Guo, D., Mazumdar, S., Dixit, S., Kajzar, F., Jarka, F., Kawabe, Y., and Peyghambarian, N. *Physical Review B* **48**(3), 1433–1459 (1993).

[94] Al Jalali, S. and Weiser, G. *Journal of Non-Crystalline Solids* **41**, 1–12 (1980).

[95] Weiser, G. *Journal of Applied Physics* **43**, 5028–5033 (1972).

[96] Feller, F. and Monkman, A. *Physical Review B* **60**(11), 8111–8116 (1999).

[97] Horowitz, G. *Journal of Materials Research* **19**(07), 1946–1962 March (2011).

[98] Castro, A., Appel, H., Oliveira, M., Rozzi, C. a., Andrade, X., Lorenzen, F., Marques, M. a. L., Gross, E. K. U., and Rubio, A. *Physica Status Solidi (B)* **243**(11), 2465–2488 September (2006).

[99] Perdew, J., Burke, K., and Ernzerhof, M. *Physical review letters* **77**(18), 3865–3868 October (1996).

[100] Perdew, J., Burke, K., and Ernzerhof, M. *Physical review letters* **78**, 1396 (E) October (1997).

[101] Wilson, J. and Di Ventra, M. *(unpublished)* .

[102] Yuen, J. D., Fan, J., Seifter, J., Lim, B., Hufschmid, R., Heeger, A. J., and Wudl, F. *Journal of the American Chemical Society* **133**(51), 20799–807 December (2011).

[103] Sonar, P., Singh, S. P., Li, Y., Soh, M. S., and Dodabalapur, A. *Advanced materials* **22**(47), 5409–13 December (2010).

[104] Lee, J., Cho, S., Seo, J. H., Anant, P., Jacob, J., and Yang, C. *Journal of Materials Chemistry* **22**(4), 1504 (2012).

[105] Zhang, Y., Kim, C., Lin, J., and Nguyen, T.-Q. *Advanced Functional Materials* **22**(1), 97–105 January (2012).

[106] Ha, T.-J., Sonar, P., Cobb, B., and Dodabalapur, A. *Organic Electronics* **13**(1), 136–141 January (2012).

[107] Tautz, R., Da Como, E., Limmer, T., Feldmann, J., Egelhaaf, H.-J., von Hauff, E., Lemaur, V., Beljonne, D., Yilmaz, S., Dumsch, I., Allard, S., and Scherf, U. *Nature communications* **3**, 970 January (2012).

[108] Khatib, O., Yuen, J. D., Wilson, J., Kumar, R., Di Ventra, M., Heeger, A. J., and Basov, D. N. *Physical Review B* **86**(19), 195109 November (2012).

[109] Yan, Y., Sun, Q.-J., Gao, X., Deng, P., Zhang, Q., and Wang, S.-D. *Applied Physics Letters* **103**(7), 073303 (2013).

[110] Di Pietro, R., Fazzi, D., Kehoe, T. B., and Sirringhaus, H. *Journal of the American Chemical Society* **134**(36), 14877–89 September (2012).

[111] Di Pietro, R. and Sirringhaus, H. *Advanced materials* **24**(25), 3367–72 July (2012).

[112] Chin, X. Y., Yin, J., Wang, Z., Caironi, M., and Soci, C. *Scientific reports* **4**, 3626 January (2014).

[113] Stallinga, P. and Gomes, H. *Synthetic Metals* **156**(21-24), 1305–1315 December (2006).

[114] Movasaghi, Z., Rehman, S., and ur Rehman, D. I. *Applied Spectroscopy Reviews* **43**(2), 134–179 February (2008).

[115] Juszczyk, P., Koodziejczyk, A. S., and Grzonka, Z. *J. Pept. Sci.* **15**, 23 (2009).

[116] Ami, D., Mereghetti, P., and Doglia, S. M. (2012).

[117] Gucciardi, P. G. In *Applied Scanning Probe Methods, Vol XII,* Bhushan, B. and Fuchs, H., editors, chapter 11, 49–66. Springer, Berlin (2009).

[118] Hillenbrand, R., Knoll, B., and Keilmann, F. *Journal of microscopy* **202**(Pt 1), 77–83 April (2001).

[119] Keilmann, F. and Hillenbrand, R. *Philosophical transactions. Series A, Mathematical, physical, and engineering sciences* **362**(1817), 787–805 April (2004).

[120] Giuseppe, P., Guillaume, G., Stephan, B., and Allegrini, M. In *Applied Scanning Probe Methods, Vol VIII*, chapter 1, 1–29. Springer, Berlin (2008).

[121] Keilmann, F. and Amarie, S. *Journal of Infrared, Millimeter, and Terahertz Waves* **33**(5), 479–484 April (2012).

[122] Huth, F., Schnell, M., Wittborn, J., Ocelic, N., and Hillenbrand, R. *Nature Materials* **10**(5), 352–356 (2011).

[123] Dai, S., Fei, Z., Ma, Q., Rodin, a. S., Wagner, M., McLeod, a. S., Liu, M. K., Gannett, W., Regan, W., Watanabe, K., Taniguchi, T., Thiemens, M., Dominguez, G., Castro Neto, a. H., Zettl, a., Keilmann, F., Jarillo-Herrero, P., Fogler, M. M., and Basov, D. N. *Science (New York, N.Y.)* **343**(6175), 1125–9 March (2014).

[124] Brehm, M., Taubner, T., Hillenbrand, R., and Keilmann, F. *Nano letters* **6**(7), 1307–10 July (2006).

[125] Amenabar, I., Poly, S., Nuansing, W., Hubrich, E. H., Govyadinov, A. a., Huth, F., Krutokhvostov, R., Zhang, L., Knez, M., Heberle, J., Bittner, A. M., and Hillenbrand, R. *Nature communications* **4**, 2890 January (2013).

[126] Berweger, S., Nguyen, D. M., Muller, E. a., Bechtel, H. a., Perkins, T. T., and Raschke, M. B. *Journal of the American Chemical Society* **135**(49), 18292–5 December (2013).

[127] Zhong, L., Zeng, G., Lu, X., Wang, R. C., Gong, G., Yan, L., Huang, D., and Chen, Z. W. *PloS one* **4**(6), e5945 January (2009).

[128] Hu, M., Chen, J., Wang, J., Wang, X., Ma, S., Cai, J., Chen, C. Y., and Chen, Z. W. *Journal of molecular recognition : JMR* **22**(6), 516–20 (2009).

[129] Dickenson, N. E., Armendariz, K. P., Huckabay, H. a., Livanec, P. W., and Dunn, R. C. *Analytical and bioanalytical chemistry* **396**(1), 31–43 January (2010).

[130] Lewis, a., Radko, a., Ben Ami, N., Palanker, D., and Lieberman, K. *Trends in cell biology* **9**(2), 70–3 February (1999).

[131] Edidin, M. *Traffic (Copenhagen, Denmark)* **2**(11), 797–803 November (2001).

[132] de Lange, F., Cambi, a., Huijbens, R., de Bakker, B., Rensen, W., Garcia-Parajo, M., van Hulst, N., and Figdor, C. G. *Journal of cell science* **114**(Pt 23), 4153–60 December (2001).

[133] Hinterdorfer, P., Garcia-Parajo, M. F., and Dufrêne, Y. F. *Accounts of chemical research* **45**(3), 327–36 March (2012).

[134] Kapkiai, L. K., Moore-Nichols, D., Carnell, J., Krogmeier, J. R., and Dunn, R. C. *Applied Physics Letters* **84**(19), 3750 (2004).

[135] van Zanten, T., Cambi, A., and Garcia-Parajo, M. *Biochimica et Biophysica Acta ...* **1798**(4), 777–787 (2010).

[136] Dunn, R. C. *Chemical reviews* **99**(10), 2891–928 October (1999).

[137] Herrmann, M., Neuberth, N., Wissler, J., Pérez, J., Gradl, D., and Naber, A. *Nano Letters* **9**(9), 3330–3336 (2009).

[138] Xu, K., Cao, P., and Heath, J. R. *Science (New York, N.Y.)* **329**(5996), 1188–91 September (2010).

[139] He, K. T., Wood, J. D., Doidge, G. P., Pop, E., and Lyding, J. W. *Nano letters* **12**(6), 2665–72 June (2012).

[140] Wood, J., Schmucker, S., Haasch, R., Doidge, G., Nienhaus, L., Damhorst, G., Lyons, A., Gruebele, M., Bashir, R., Pop, E., and Lyding, J. *2012 12th IEEE International Conference on Nanotechnology (IEEE-NANO)* , 1–4 (2012).

[141] Novoselov, K., Fal'ko, V. I., Colombo, L., Gellet, P., Schwab, M. G., and Kim, K. *Nature* **487**, 82 (2012).

[142] Basov, D., Fogler, M., Lanzara, a., Wang, F., and Zhang, Y. *Reviews of Modern Physics* **86**(3), 959–994 July (2014).

[143] Wang, C., Qiao, Q., Shokuhfar, T., and Klie, R. F. *Advanced materials (Deerfield Beach, Fla.)* **26**(21), 3410–4 June (2014).

[144] Wood, J. D. *Large-scale growth, fluorination, clean transfer, and layering of graphene and related nanomaterials*. PhD thesis, (2013).

[145] Ocelic, N., Huber, A., and Hillenbrand, R. *Applied Physics Letters* **89**(10), 101124 (2006).

[146] Gambetta, A., Ramponi, R., and Marangoni, M. *Optics letters* **33**(22), 2671–3 November (2008).

[147] Trinh, M.-H., Odorico, M., Bellanger, L., Jacquemond, M., Parot, P., and Pellequer, J.-L. *Journal of molecular recognition : JMR* **24**(3), 503–10 (2011).

[148] Alonso, J. M., Górzny, M. ., and Bittner, a. M. *Trends in biotechnology* **31**(9), 530–8 September (2013).

[149] Fei, Z., Rodin, A. S., Gannett, W., Dai, S., Regan, W., Wagner, M., Liu, M. K., Mcleod, A. S., Dominguez, G., Thiemens, M., Neto, A. H. C., Keilmann, F., Zettl, A., Hillenbrand, R., Fogler, M. M., and Basov, D. N. *Nature Nanotechnology* **8**(October), 821–825 (2013).

[150] Huth, F., Govyadinov, A., Amarie, S., Nuansing, W., Keilmann, F., and Hillenbrand, R. *Nano letters* **12**(8), 3973–8 August (2012).

[151] Bertie, J. E., Ahmed, M. K., and Eysel, H. H. *J. Phys. Chem.* **93**(16), 2210–2218 (1989).

[152] Liang, J.-i., Hawthorne, F. C., and Swainson, I. A. N. P. *The Canadian Mineralogist* **36**, 1017–1027 (1998).

[153] Hillenbrand, R., Taubner, T., and Keilmann, F. *Nature* **418**(6894), 159–62 July (2002).

[154] Andreas, J. *Nanoscale Surface-Polariton Spectroscopy by Mid- and Far-Infrared Near-Field Microscopy*. PhD thesis, (2009).

[155] Zhang, L. M., Andreev, G. O., Fei, Z., McLeod, a. S., Dominguez, G., Thiemens, M., Castro-Neto, a. H., Basov, D. N., and Fogler, M. M. *Physical Review B* **85**(7), 075419 February (2012).

[156] Hale, G. M. and Querry, M. R. *Applied optics* **12**(3), 555–63 March (1973).

[157] Vedder, W. *American Mineralogist* **19**, 736–768 (1964).

[158] Herzinger, C., Johs, B., MacGahan, W., Woollam, J., and Paulson, W. *Journal of Applied Physics* **83**(6), 3323–3336 (1998).

[159] Fei, Z., Andreev, G. O., Bao, W., Zhang, L. M., S McLeod, A., Wang, C., Stewart, M. K., Zhao, Z., Dominguez, G., Thiemens, M., Fogler, M. M., Tauber, M. J., Castro-Neto, A. H., Lau, C. N., Keilmann, F., and Basov, D. N. *Nano letters* **11**(11), 4701–5 November (2011).

[160] Mcleod, A. S., Kelly, P., Goldflam, M. D., Gainsforth, Z., Westphal, A. J., Dominguez, G., Thiemens, M. H., Fogler, M. M., and Basov, D. N. *arXiv:1308.1784v2* , 1–18 (2013).

[161] Fei, Z., Rodin, a. S., Andreev, G. O., Bao, W., McLeod, a. S., Wagner, M., Zhang, L. M., Zhao, Z., Thiemens, M., Dominguez, G., Fogler, M. M., Castro Neto, a. H., Lau, C. N., Keilmann, F., and Basov, D. N. *Nature* **487**(7405), 82–5 July (2012).